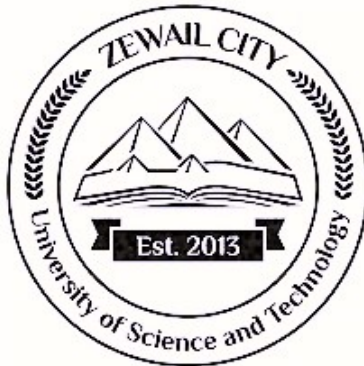


UNDERGRADUATE PROJECT
UNIVERSITY OF SCIENCE AND TECHNOLOGY IN
ZEWAIL CITY



**Department of Nanotechnology and
Nanoelectronics Engineering**

P-N JUNCTIONS

Authors:

Rawan Mahmoud¹
Mahitab Swid²

INSTRUCTOR: Prof . NOHA GABER

Academic year 2024/2025

¹Sophomore student at Nanotechnology and Nanoelectronics Department, UST ZC: ID 202301012
²Sophomore student at Nanotechnology and Nanoelectronics Department, UST ZC: ID 202300410

CONTENTS

| | |
|--|-----------|
| Contents | 3 |
| 1 THEORETICAL INVESTIGATIONS OF P-N JUNCTIONS IN SEMICONDUCTORS | 1 |
| 1 INTRODUCTION | 1 |
| 1.1 BACKGROUND | 1 |
| 1.2 OBJECTIVES | 1 |
| 1.3 THE STRUCTURE OF OUR APPROACH | 2 |
| 2 THEORY OF P-N JUNCTIONS | 2 |
| 2.1 FORMATION OF THE JUNCTION | 2 |
| 2.2 ELECTRICAL CHARACTERISTICS | 5 |
| 2.3 ENERGY BAND DIAGRAM | 6 |
| 3 APPLICATIONS OF P-N JUNCTIONS | 7 |
| 3.1 DIODES | 7 |
| 3.2 TRANSISTORS | 8 |
| 3.3 PHOTOVOLTAIC CELLS | 10 |
| 4 BUILT-IN VOLTAGE (V_{bi}) | 11 |
| 4.1 DEFINITION AND IMPORTANCE | 11 |
| 4.2 MATHEMATICAL FORMULATION | 12 |
| 4.3 PHYSICAL INTERPRETATION | 14 |
| 5 ANALYTICAL MODELING OF P-N JUNCTIONS | 15 |
| 5.1 POISSON'S EQUATION | 15 |
| 5.2 CHARGE DENSITY AND ELECTRIC FIELD | 16 |
| 5.3 CURRENT-VOLTAGE CHARACTERISTICS | 17 |
| 6 CONCLUSION | 18 |
| 2 COMPREHENSIVE SIMULATIONS | 20 |
| 1 SIMULATION OBJECTIVES | 20 |
| 2 COMSOL MODEL SETUP | 20 |
| 3 SILICON | 21 |
| 3.1 OVERVIEW | 21 |
| 3.2 SILICON SIMULATION RESULTS | 21 |
| 3.3 DISCUSSION | 24 |
| 4 GaAs | 25 |
| 4.1 OVERVIEW | 25 |
| 4.2 GaAs SIMULATION RESULTS | 26 |
| 4.3 DISCUSSION | 28 |
| 5 AlGaAs | 28 |
| 5.1 OVERVIEW | 28 |
| 5.2 AlGaAs SIMULATION RESULTS | 29 |
| 5.3 DISCUSSION | 31 |

| | | |
|-----|---|----|
| 6 | DIAMOND | 32 |
| 6.1 | OVERVIEW | 32 |
| 6.2 | SIMULATION RESULTS | 32 |
| 6.3 | Discussion | 35 |
| 7 | COMPARATIVE ANALYSIS AND THEORETICAL INTERPRETATION | 35 |
| 8 | CONCLUSION | 36 |
| | Bibliography | 38 |

CHAPTER 1

THEORETICAL INVESTIGATIONS OF P-N JUNCTIONS IN SEMICONDUCTORS

1 INTRODUCTION

1.1 BACKGROUND

P-n junctions are the foundational element of semiconductor devices, enabling the directional control of electric current in nearly all modern electronic circuits. They are created by joining p-type and n-type semiconductor materials, resulting in a junction that exhibits nonlinear current–voltage (I–V) characteristics essential for device functions like rectification, amplification, and energy conversion (Hu, 2009).

The core functionality of the p-n junction arises from the interaction between charge carriers—holes from the p-type region and electrons from the n-type region. Upon contact, carriers diffuse across the junction, leaving behind ionized dopants and forming a depletion region. This region is depleted of mobile carriers but rich in immobile charge, giving rise to an internal electric field and a built-in potential that opposes further carrier movement (Darkwi & Elfituri, 2022; Hu, 2009). At thermal equilibrium, this built-in voltage creates a potential barrier that significantly influences device behavior under external bias.

Understanding the formation, electric field distribution, and current transport mechanisms within p-n junctions is vital not only for traditional diodes and transistors, but also for advanced applications such as nanowire devices and photovoltaic cells (Anttu et al., 2024). Analytical and numerical methods, including solutions to Poisson’s equation, continue to enhance modeling accuracy, especially in structures with nonuniform doping profiles or two-dimensional characteristics.

As device dimensions shrink and integration increases, accurate modeling of p-n junction behavior becomes increasingly important. This includes analyzing parameters like depletion width, junction capacitance, and breakdown behavior under high electric fields. Modern research also investigates non-ideal effects and nanoscale behaviors that deviate from classical approximations, necessitating comprehensive theoretical and experimental study.

1.2 OBJECTIVES

This work aims to provide a comprehensive analysis of the p-n junction, integrating theoretical modeling with numerical simulation. The primary goals are to explain the physical theory behind p-n junction formation, including charge carrier dynamics, depletion region behavior, and the concept of built-in voltage (V_{bi}); to discuss key applications of p-n junctions in modern electronics, such as diodes, transistors, and photovoltaic cells; and to derive and analyze the

analytical models that describe charge density, electric field, and current-voltage characteristics using Poisson's equation and drift-diffusion theory.

Furthermore, we aim to implement a two-dimensional model of a p-n junction in COMSOL Multiphysics, simulate its I-V behavior under forward bias, and compare it with analytical predictions. The study will examine the effect of doping concentration (from 10^{14} to 10^{19} cm^{-3}) on V_{bi} and I-V characteristics, using symmetrical doping in both junction regions. Additionally, we will compare the I-V responses of three different semiconductor materials under identical doping conditions and discuss how material properties influence performance. All simulation results will be evaluated against theoretical expectations, with discrepancies explained using appropriate modeling equations and known sources of numerical error.

To summarize the objectives, we have:

- (i) To explain the physical theory behind p-n junction formation, including charge carrier dynamics, depletion region behavior, and the concept of built-in voltage (V_{bi})
- (ii) To discuss key applications of p-n junctions in modern electronics, such as diodes, transistors, and photovoltaic cells
- (iii) To derive and analyze the analytical models that describe charge density, electric field, and current-voltage characteristics using Poisson's equation and drift-diffusion theory
- (iv) To implement a two-dimensional model of a p-n junction in COMSOL Multiphysics, simulate its I-V behavior under forward bias, and compare it with analytical predictions
- (v) To study the effect of doping concentration (from 10^{14} to 10^{19} cm^{-3}) on V_{bi} and I-V characteristics, using symmetrical doping in both junction regions
- (vi) To compare the I-V responses of three different semiconductor materials under identical doping conditions and discuss how material properties influence performance
- (vii) To evaluate all simulation results against theoretical expectations and explain discrepancies using appropriate modeling equations and known sources of numerical error

This combined approach aims to bridge textbook theory with practical simulation insight, helping validate analytical tools while demonstrating their limitations in real-world modeling scenarios.

1.3 THE STRUCTURE OF OUR APPROACH

This work is organized into six main sections. Section 2 presents the fundamental theory of p-n junctions, including their formation, electrical characteristics, and energy band behavior. Section 3 covers the primary applications of p-n junctions in electronic and optoelectronic devices. Section 4 explains the concept of built-in voltage (V_{bi}), its mathematical derivation, and physical relevance. Section 5 develops the analytical modeling framework based on Poisson's equation and carrier transport equations. Section 6 concludes with a summary of findings and the significance of p-n junctions in semiconductor device design. The reference section lists all sources used.

2 THEORY OF P-N JUNCTIONS

2.1 FORMATION OF THE JUNCTION

BASIC STRUCTURE OF A P–N JUNCTION SHOWING THE DEPLETION REGION FORMED AT THE INTERFACE. A p-n junction is formed by joining p-type and n-type semiconductors—materials

doped with acceptor and donor atoms, respectively. This creates a boundary where mobile charge carriers—holes from the p-side and electrons from the n-side—diffuse into the opposite region and recombine. The result is the formation of a depletion region, a zone devoid of free carriers but rich in fixed ionized dopants (Hu, 2009, pp. 89–91), as shown in Figure 1.1.

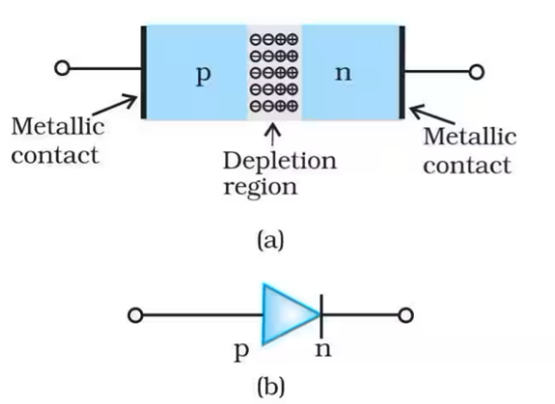


Figure 1.1: PN Junction Structure: Basic structure of a p–n junction showing the depletion region formed at the interface.

As this diffusion occurs, it leaves behind positively charged donor ions in the n-region and negatively charged acceptor ions in the p-region, as shown in Figure 1.2. These fixed charges generate an internal electric field that opposes further carrier diffusion. Eventually, equilibrium is reached when the drift of carriers due to the electric field balances their diffusion. This equilibrium condition establishes the built-in potential, V_{bi} , across the junction (Hu, 2009, p. 92):

$$V_{bi} = \frac{kT}{q} \ln \left(\frac{N_D N_A}{n_i^2} \right) \quad (1.1)$$

where N_D and N_A are the donor and acceptor concentrations (cm^{-3}), n_i is the intrinsic carrier concentration (cm^{-3}), k is Boltzmann's constant ($1.38 \times 10^{-23} \text{ J/K}$), T is temperature (K), and q is the elementary charge ($1.6 \times 10^{-19} \text{ C}$).

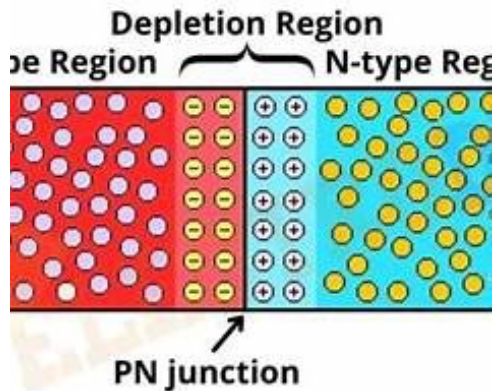


Figure 1.2: Fixed Charge Distribution: Carrier diffusion creates fixed charges, resulting in an internal electric field across the junction.

The spatial distribution of electric field and potential within the depletion layer is governed by Poisson's equation:

$$\frac{d^2V}{dx^2} = -\frac{\rho(x)}{\varepsilon_s} \quad (1.2)$$

where $\rho(x)$ is the charge density (C/cm^3) and ε_s is the semiconductor permittivity (F/cm). In the idealized abrupt junction, $\rho(x) = qN_D$ for $0 < x < x_n$ and $\rho(x) = -qN_A$ for $-x_p < x < 0$, resulting in a triangular electric field profile that peaks at the junction ($x = 0$) as shown in Figure 1.3.

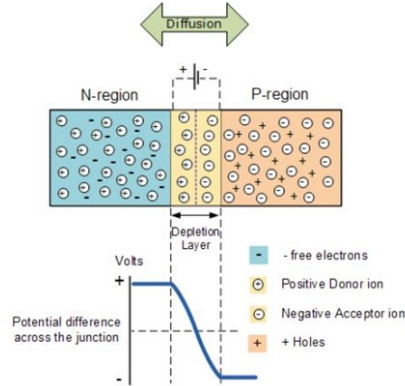


Figure 1.3: Electric Field and Potential Profiles: Electric field and potential variation across the depletion layer, derived from Poisson's equation.

The three-dimensional form of *Poisson's equation* is given by:

$$\nabla^2 V \equiv \frac{\partial^2 V}{\partial x^2} + \frac{\partial^2 V}{\partial y^2} + \frac{\partial^2 V}{\partial z^2} = -\frac{\rho(x, y, z)}{\varepsilon_s} \quad (1.3)$$

This Laplacian formulation becomes essential when analyzing non-planar junctions or edge effects in real devices, where the potential varies in all three spatial dimensions. The equation reduces to the one-dimensional form Equation(1.2) for ideal planar junctions with translational symmetry in the $y - z$ plane.

The total depletion width $W_{dep} = x_n + x_p$ is determined by solving Equation 1.2 with appropriate boundary conditions:

$$W_{dep} = \sqrt{\frac{2\varepsilon_s V_{bi}}{q} \left(\frac{1}{N_A} + \frac{1}{N_D} \right)} \quad (1.4)$$

The junction is often asymmetrical; in such cases, the depletion region penetrates primarily into the more lightly doped side (Hu, 2009, p. 96).

More realistic modeling must consider non-uniform doping. As shown by Darkwi and Elfituri (2022), solving Poisson's equation numerically for a linearly graded junction reveals that the electric field and potential profiles deviate significantly from the ideal case, especially near the metallurgical junction where the doping gradient introduces curvature in the field distribution.

Historically, the first p-n junction behavior was discovered unintentionally. In 1940, Russell Ohl observed photovoltaic effects in a silicon rod cut across two regions with different impurity concentrations, forming what turned out to be a natural p-n junction (Riordan & Hoddeson, 1997). This serendipitous discovery laid the foundation for modern semiconductor electronics, eventually enabling the development of transistors and solar cells.

2.2 ELECTRICAL CHARACTERISTICS

The p-n junction exhibits nonlinear electrical behavior, which is essential to its function in electronic devices. Its current–voltage (I–V) relationship changes depending on the direction of applied bias. Figure 1.4 shows the current–voltage relationship in the junction of a diode.

In forward bias, a positive voltage is applied to the p-side relative to the n-side. This lowers the built-in potential barrier from ϕ_{bi} to $(\phi_{bi} - V)$, allowing charge carriers to diffuse across the junction. This results in minority carrier injection, where electrons move into the p-side and holes into the n-side (Hu, 2009, p. 105). The forward current increases exponentially with applied voltage and follows the ideal diode equation:

$$I = I_s \left(\exp \left(\frac{qV}{kT} \right) - 1 \right) \quad (1.5)$$

where I is the diode current, I_s is the reverse saturation current, q is the elementary charge, V is the applied voltage, k is Boltzmann's constant, and T is the absolute temperature in Kelvin.

**Graphical
PN-Junction Diode V-I Characteristic**

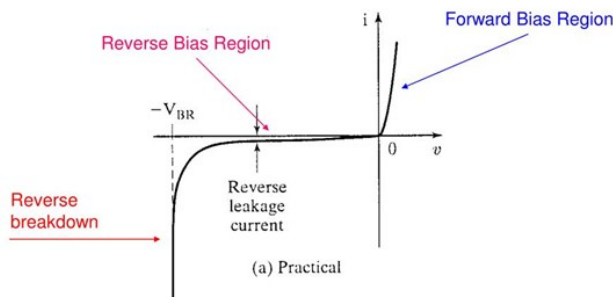


Figure 1.4: Diode I–V Characteristics: Current–voltage curve of a p–n junction diode showing forward and reverse bias behavior.

Under reverse bias, the voltage is applied in the opposite direction (n-side more positive). This increases the potential barrier to $(\phi_{bi} + V_r)$, widens the depletion region, and suppresses carrier injection (Hu, 2009, p. 97). The resulting current is very small and approximately equal to I_s .

When reverse bias is increased further, the junction may undergo breakdown via:

1. Avalanche breakdown, where energetic carriers create more pairs through impact ionization (Hu, 2009, pp. 103–104).
2. Zener (tunneling) breakdown, in heavily doped junctions with narrow depletion widths (Hu, 2009, p. 102).

The peak electric field at breakdown:

$$E_{peak} = \sqrt{\frac{2qN(\phi_{bi} + V)}{\varepsilon_s}} \quad (1.6)$$

The breakdown voltage is:

$$V_B \approx \frac{\varepsilon_s E_{crit}^2}{2qN} \quad (1.7)$$

where E_{crit} is typically around 5×10^5 V/cm for silicon.

At high injection levels, the ideal diode law fails. As Cristea (2011) describes, both majority and minority carrier concentrations exceed equilibrium values. His unified model modifies boundary conditions to describe both low and high injection regimes more accurately.

2.3 ENERGY BAND DIAGRAM

At thermal equilibrium, the Fermi level (E_F) is constant across the p-n junction. The conduction band (E_C) and valence band (E_V) bend near the junction due to the built-in electric field, forming a potential barrier (Hu, 2009, pp. 90–91).

The built-in potential ϕ_{bi} is:

$$\phi_{bi} = \frac{kT}{q} \ln \left(\frac{N_D N_A}{n_i^2} \right) \quad (1.8)$$

The depletion widths satisfy:

$$N_A x_P = N_D x_N \quad (1.9)$$

$$W_{dep} = x_P + x_N = \sqrt{\frac{2\epsilon_s \phi_{bi}}{q} \left(\frac{1}{N_A} + \frac{1}{N_D} \right)} \quad (1.10)$$

Under forward bias, the barrier is reduced; under reverse bias, it's increased. Band diagrams – as the one shown in Figure 1.16 – help visualize carrier transport and are essential for understanding optoelectronic effects like the photovoltaic effect.

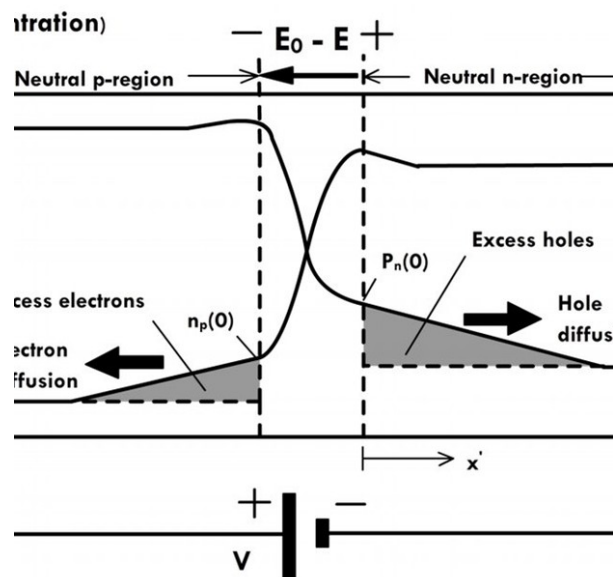


Figure 1.5: Energy Band Diagram at Equilibrium: Band diagram illustrating energy levels, carrier concentrations, and built-in potential at equilibrium.

3 APPLICATIONS OF P-N JUNCTIONS

3.1 DIODES

The p-n junction diode (Figure 1.6) acts as a one-way current valve. In forward bias, current flows readily; in reverse bias, it is blocked (Hu, 2009, p. 90; Kishore, n.d., p. 1).

Rectifier diodes are used in AC-DC conversion circuits:

- Half-Wave Rectifier (HWR)
- Full-Wave Rectifier (FWR)
- Bridge Rectifier

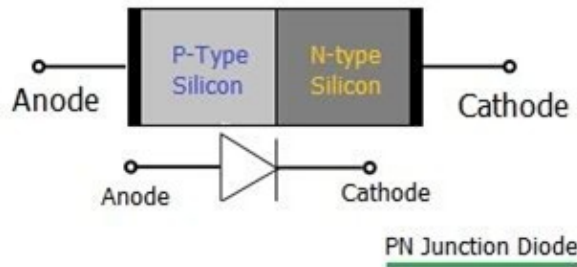


Figure 1.6: P-N Junction Structure and Corresponding Diode Symbol: Physical and circuit symbol representation of a p-n junction acting as a diode.

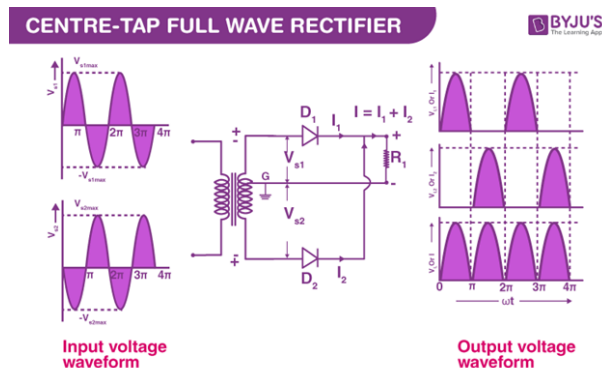


Figure 1.7: Full-Wave Rectifier Circuit: Full-wave rectifier using two diodes with corresponding input and output voltage waveforms.

Zener diodes operate in reverse breakdown mode to regulate voltage, leading to a curve as shown in the graph in Figure 1.8

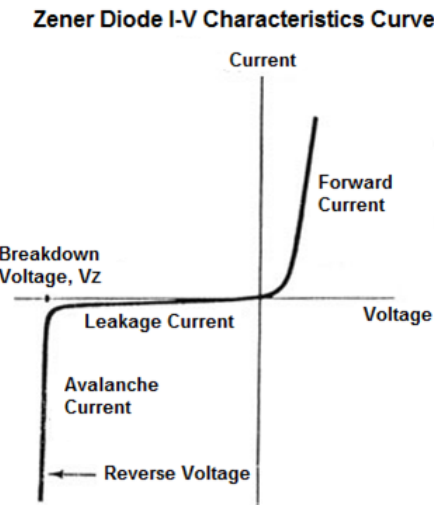


Figure 1.8: Zener Diode Characteristics: I^V curve of a *Zener diode* showing breakdown behavior under reverse bias.

LEDs emit light during electron-hole recombination in a forward-biased junction, using materials like GaAs or GaN for efficient photon emission (Hu, 2009, p. 89). The current-voltage relationship under forward bias is shown in Figure 1.9.

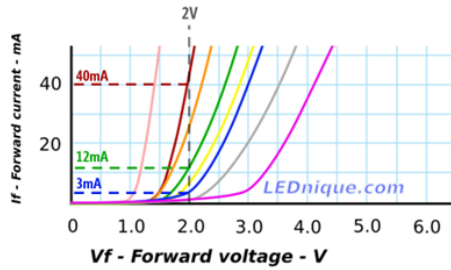


Figure 1.9: LED Forward Bias Characteristics: Current–voltage characteristics of LEDs using different materials in forward bias.

3.2 TRANSISTORS

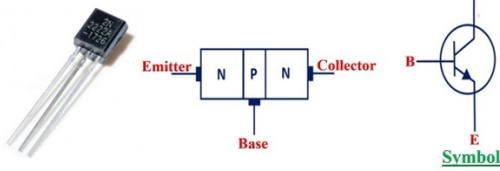
BJTs have three terminals: emitter, base, and collector, as shown in Figure 1.10. An npn BJT consists of two p-n junctions. The collector current I_C is related to base current I_B by:

$$I_C = \beta I_B \quad (1.11)$$

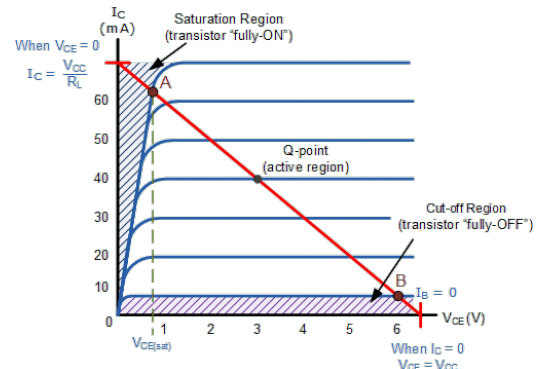
$$I_E = I_C + I_B \quad (1.12)$$

BJTs operate in cutoff, active, and saturation regions, as shown in Figure 1.10b. They are used in switches, amplifiers, and digital logic (Chaniotakis & Cory, 2006, pp. 1–9).

Bipolar Junction Transistor (BJT)



(a) (a) BJT Structure and Symbol: Construction and symbol of a bipolar junction transistor composed of two p–n junctions.



(b) BJT Output Characteristics Collector current I_{C1_C} vs. collector-emitter voltage V_{CE_CE} characteristics showing cutoff, active, and saturation regions of BJT operation along with the load line and Q-point.

Figure 1.10: BJT characteristics: (a) physical structure and (b) operating regions.

MOSFETs are unipolar, voltage-controlled devices. The drain current in the linear region is given by:

$$I_D = \frac{W}{L} \mu_n C_{ox} \left[(V_{GS} - V_T)V_{DS} - \frac{V_{DS}^2}{2} \right] \quad (1.13)$$

In saturation region, the current becomes:

$$I_{Dsat} = \frac{1}{2} \frac{W}{L} \mu_n C_{ox} (V_{GS} - V_T)^2 \quad (1.14)$$

These transistors dominate VLSI technology due to their low power consumption and high scalability (MIT, 2007).

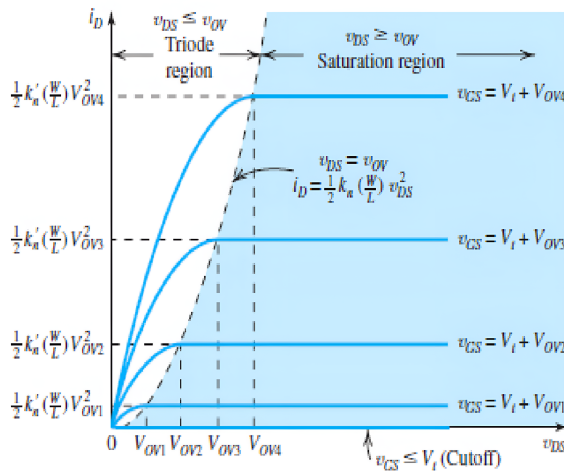


Figure 1.11: MOSFET Output Characteristics Current–voltage characteristics of an n-channel MOSFET showing transition from the triode region to saturation for various gate voltages $V_{GS}V_{GS}$, with quadratic dependence in saturation.

3.3 PHOTOVOLTAIC CELLS

Solar cells use a p-n junction to convert sunlight into electricity via the photovoltaic effect, as Figure 1.12 shows. When photons with energy $h\nu \geq E_g$ are absorbed, electron-hole pairs are generated and separated by the junction's electric field, generating a photocurrent (Lecture 22 Solar Cells ATL.pdf, slide).

The illuminated I-V equation:

$$I = I_0 \left(\exp \left(\frac{qV}{kT} \right) - 1 \right) - I_{ph} \quad (1.15)$$

Key parameters include the short-circuit current (J_{sc}), open-circuit voltage (V_{oc}), and efficiency $\eta = (V_{mp}J_{mp}FF)/P_{opt}$.

Silicon is the most used material. Surface texturing, antireflection coatings, and doping profiles are used to optimize light capture and carrier collection. Advanced technologies include tandem cells, light concentrators, and thin films such as amorphous silicon (a-Si), cadmium telluride (CdTe), and copper indium gallium selenide (CIGS).

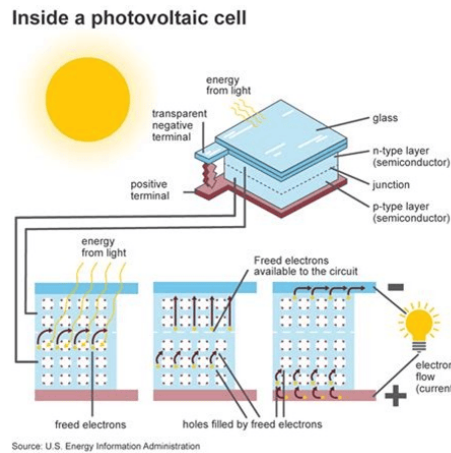


Figure 1.12: Photovoltaic Cell Operation:Structure of a solar cell showing carrier separation and photocurrent generation via the p–n junction.

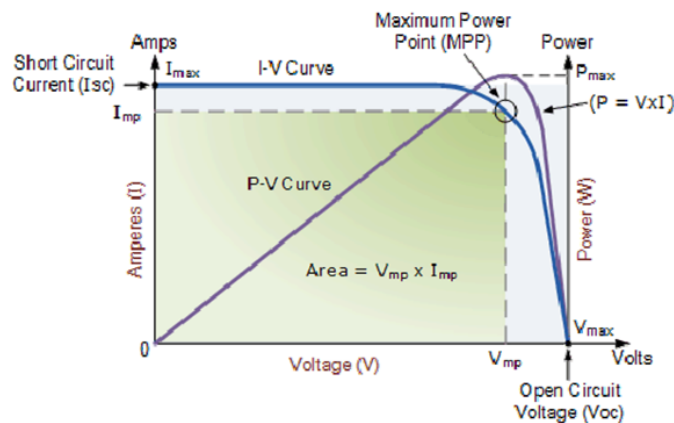


Figure 1.13: Solar Cell I-V and P-V Curves: I-V and power–voltage characteristics of a solar cell showing the maximum power point (MPP) and output parameters

4 BUILT-IN VOLTAGE (V_{bi})

4.1 DEFINITION AND IMPORTANCE

The built-in voltage (also called the contact potential or junction potential) is the electrostatic potential that naturally forms across a p-n junction under equilibrium conditions. It results from the diffusion of majority carriers—electrons from the n-type side and holes from the p-type side—across the junction interface. As these carriers recombine, they leave behind fixed ionized dopants, creating a region void of mobile charge known as the depletion region (Lec10.pdf, pp. 3–4; Hu, 2009, p. 91).

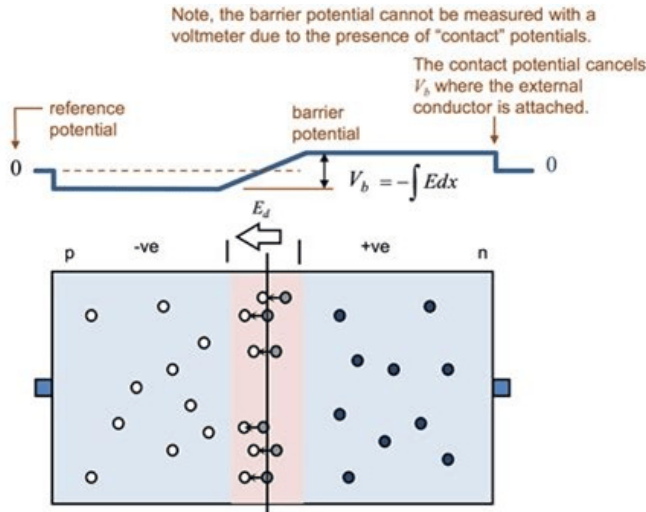


Figure 1.14: – Built-in Potential Formation: Illustration of the internal electric field and potential barrier (V_{bi}) formed due to fixed charges in the depletion region

Figure 1.14 shows that this fixed charge gives rise to an internal electric field pointing from the n-side to the p-side. This field opposes further diffusion, and when drift and diffusion balance, the system reaches thermal equilibrium. The resulting potential barrier is the built-in voltage, V_{bi} .

The built-in potential aligns the Fermi levels across the junction and determines the energy band bending near the interface. It is central to the junction's ability to control current flow, and influences key parameters such as depletion width, capacitance, junction response time, and carrier collection efficiency in devices like diodes, transistors, and solar cells.

For example, in a silicon junction with $N_A = 2 \times 10^{16} \text{ cm}^{-3}$ and $N_D = 1 \times 10^{16} \text{ cm}^{-3}$, the built-in potential is approximately 0.73 V at room temperature (Lec10.pdf, p. 10). This value increases for materials with lower intrinsic carrier concentration, such as GaAs, and decreases with temperature due to the exponential increase in n_i .

In practice:

- A forward bias reduces V_{bi} , narrowing the depletion region and allowing current flow.
- A reverse bias increases V_{bi} , widening the depletion region and suppressing current.
- In photovoltaic cells, V_{bi} separates photo-generated carriers, generating usable current.

V_{bi} is thus essential in defining the electrostatic environment of a junction and controlling its electrical behavior.

4.2 MATHEMATICAL FORMULATION

The equilibrium analysis of step junctions begins with the built-in voltage V_{bi} . The intrinsic Fermi level E_i , which represents the energy level at the center of the band gap, plays a crucial role in determining this potential. The relationship is given by:

$$qV_{bi} = (E_i - E_F)_p + (E_F - E_i)_n \quad (1.16)$$

The equilibrium carrier concentrations on either side of the junction are expressed in terms of E_i and the Fermi level E_F . For the n-type material, the majority electron concentration is:

$$n_{n0} = n_i \exp\left(\frac{E_F - E_i}{k_B T}\right) \quad (1.17)$$

while for the p-type material, the majority hole concentration is:

$$p_{p0} = n_i \exp\left(\frac{E_i - E_F}{k_B T}\right) \quad (1.18)$$

The built-in voltage can be calculated from these concentrations or directly from the doping levels N_A and N_D :

$$V_{bi} = \frac{k_B T}{q} \ln\left(\frac{p_{p0} n_{n0}}{n_i^2}\right) \approx V_T \ln\left(\frac{N_A N_D}{n_i^2}\right) \quad (1.19)$$

where $V_T = k_B T/q$ is the thermal voltage. The relationship between majority and minority carriers at equilibrium is characterized by:

$$p_{n0} = p_{p0} \exp\left(-\frac{V_{bi}}{V_T}\right) \quad (1.20)$$

for the minority hole concentration on the n-side, and:

$$n_{p0} = n_{n0} \exp\left(-\frac{V_{bi}}{V_T}\right) \quad (1.21)$$

These equations describe the fundamental equilibrium properties of a p-n junction, with E_i serving as the reference energy level throughout the analysis.

I. CARRIER CONCENTRATION-BASED DERIVATION At equilibrium, the law of mass action holds:

$$n(x) \cdot p(x) = n_i^2 \quad (1.22)$$

Where n_i is the intrinsic carrier concentration. Using equilibrium carrier values:

On the n-side:

$$n_n = N_D, \quad p_n = \frac{n_i^2}{N_D} \quad (1.23)$$

On the p-side:

$$p_p = N_A, \quad n_p = \frac{n_i^2}{N_A} \quad (1.24)$$

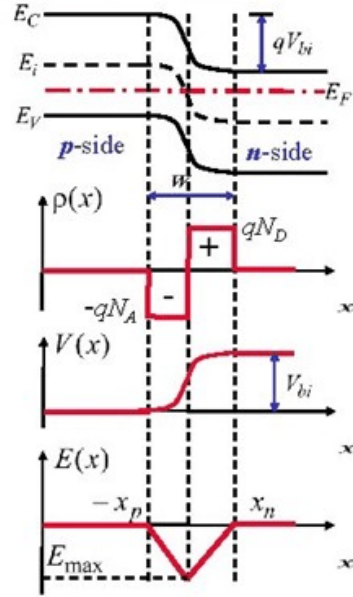


Figure 1.15: Energy Band Diagram with Carrier Distributions: Step-junction band diagram showing built-in potential derivation and majority-minority carrier concentration relationships.

The ratio of minority carrier concentrations:

$$\frac{n_p}{n_n} = \frac{n_i^2}{N_A N_D} \quad (1.25)$$

From Boltzmann statistics:

$$\frac{n_p}{n_n} = \exp\left(-\frac{qV_{bi}}{kT}\right) \quad (1.26)$$

Equating and solving:

$$V_{bi} = \frac{kT}{q} \ln\left(\frac{N_A N_D}{n_i^2}\right) \quad (1.27)$$

This equation shows V_{bi} increases with doping concentrations and decreases with higher n_i (Lec10.pdf, pp. 9-10; Hu, 2009, p. 92).

II. ELECTROSTATIC DERIVATION USING POISSON'S EQUATION In the depletion approximation, mobile carriers are neglected. The charge density $\rho(x)$ is:

$$-\rho = -qN_A \text{ for } -w_p < x < 0, \quad \rho = +qN_D \text{ for } 0 < x < w_n \quad (1.28)$$

Poisson's equation in 1D:

$$\frac{d^2V}{dx^2} = -\frac{\rho(x)}{\epsilon_s} \quad (1.29)$$

Integrating once gives electric field $E(x)$:

On the p-side:

$$E(x) = -\frac{qN_A}{\epsilon_s}(x + w_p) \quad (1.30)$$

On the n-side:

$$E(x) = \frac{qN_D}{\epsilon_s}(x - w_n) \quad (1.31)$$

Integrating again gives the potential:

$$V(x) = \frac{qN_A}{2\epsilon_s}(x + w_p)^2 \quad \text{on p-side,}$$

and

$$V(x) = V_{bi} - \frac{qN_D}{2\epsilon_s}(x - w_n)^2 \quad \text{on n-side.}$$

Total built-in voltage:

$$V_{bi} = \frac{q}{2\epsilon_s}(N_A w_p^2 + N_D w_n^2) \quad (1.32)$$

Using charge neutrality:

$$N_A w_p = N_D w_n \quad (1.33)$$

And defining total depletion width $W = w_p + w_n$:

$$w_p = \frac{N_D}{N_A + N_D} W, \quad w_n = \frac{N_A}{N_A + N_D} W \quad (1.34)$$

Then,

$$W = \sqrt{\frac{2\epsilon_s V_{bi}}{q} \left(\frac{1}{N_A} + \frac{1}{N_D} \right)} \quad (1.35)$$

These equations show the strong interdependence between electrostatics and material parameters (Lec10.pdf, pp. 6-8; Hu, 2009, pp. 93-96).

III. EXAMPLE FOR SILICON Given:

$$\begin{aligned}N_A &= 2 \times 10^{16} \text{ cm}^{-3}, \\N_D &= 1 \times 10^{16} \text{ cm}^{-3}, \\n_i &= 1.5 \times 10^{10} \text{ cm}^{-3}, \\T &= 300 \text{ K}, \\kT/q &\approx 0.0259 \text{ V}\end{aligned}$$

Then:

$$V_{bi} \approx 0.0259 \ln \left(\frac{2 \times 10^{16} \times 1 \times 10^{16}}{2.25 \times 10^{20}} \right) \approx 0.713 \text{ V} \quad (1.36)$$

Depletion width:

$$W = \sqrt{\frac{2\epsilon_s V_{bi}}{q} \left(\frac{1}{N_A} + \frac{1}{N_D} \right)} \quad (1.37)$$

For silicon ($\epsilon_s \approx 11.9\epsilon_0$), the total depletion width comes out to approximately 381 nm, with the junction extending more into the lightly doped n-side (Lec10.pdf, p. 10).

IV. PRACTICAL IMPLICATIONS

- (i) Materials like GaAs (lower n_i) produce higher V_{bi} for same doping.
- (ii) Higher doping increases V_{bi} logarithmically.
- (iii) V_{bi} decreases with increasing temperature due to higher n_i .
- (iv) V_{bi} defines carrier barrier height and thus controls diode turn-on voltage, depletion width, capacitance, and switching time.
- (v) In photovoltaic operation, it separates light-generated carriers; in reverse bias, it determines breakdown susceptibility.

4.3 PHYSICAL INTERPRETATION

V_{bi} is not just a mathematical value — it represents the electrostatic “wall” formed inside the junction. Physically, it is the energy barrier that prevents further carrier diffusion once equilibrium is established.

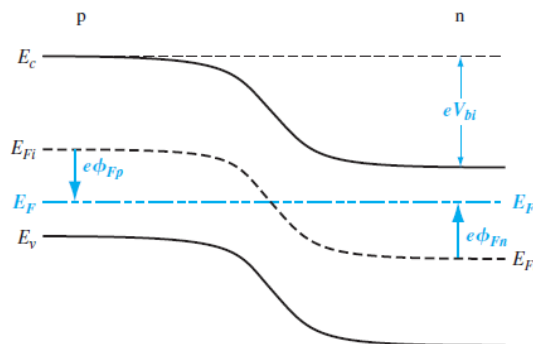


Figure 1.16: Band Diagram under Thermal Equilibrium: Conduction and valence band bending across the junction illustrates the electrostatic potential barrier and Fermi level alignment at equilibrium.

In the energy band diagram shown in Figure 1.16, the built-in voltage corresponds to the difference in conduction and valence band edges across the depletion region. The conduction band bends upward from the n-side to the p-side, reflecting the increasing potential energy for electrons. Similarly, the valence band bends downward, increasing hole potential energy from p to n. The resulting potential-position diagram is shown in Figure 1.17.

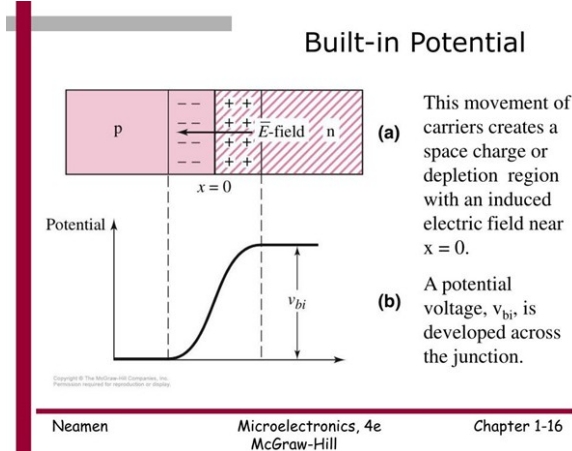


Figure 1.17: Potential and Electric Field Profile of a pn Junction: This diagram illustrates how charge separation near the junction creates an internal electric field and built-in potential, forming the basis of junction behavior.

The alignment of Fermi levels across the junction at equilibrium is the hallmark of a built-in potential — the bands must bend to achieve this alignment (Lec10.pdf, p. 11; Hu, 2009, p. 92).

Operationally:

- **Forward Bias** lowers the barrier ($V_{bi} - V_{\text{applied}}$), enabling carrier injection and large forward current.
- **Reverse Bias** increases the barrier ($V_{bi} + V_{\text{applied}}$), suppressing current and widening the depletion zone.
- **In Solar Cells**, V_{bi} acts as the field that drives photogenerated carriers to opposite sides, generating photocurrent.

In short, V_{bi} controls whether the junction resists or permits current flow, and is central to the operation of almost every semiconductor device.

5 . ANALYTICAL MODELING OF P-N JUNCTIONS

5.1 POISSON'S EQUATION

The electrostatic behavior of a p-n junction is governed by Poisson's equation, which relates the second derivative of the electrostatic potential to the local charge density:

$$\frac{d^2V}{dx^2} = -\frac{\rho(x)}{\epsilon_s} \quad (1.38)$$

where $V(x)$ is the electrostatic potential, $\rho(x)$ is the space charge density, and ϵ_s is the permittivity of the semiconductor.

Under the depletion approximation in an abrupt step junction, the charge density is:

$$\rho(x) = \begin{cases} -qN_A & \text{for } -w_p < x < 0 \\ +qN_D & \text{for } 0 < x < w_n \\ 0 & \text{elsewhere} \end{cases} \quad (1.39)$$

Here, N_A and N_D are acceptor and donor concentrations, and q is the elementary charge. By integrating Poisson's equation, the electric field in the p-side is:

$$E(x) = -\frac{qN_A}{\epsilon_s}(x + w_p) \quad (1.40)$$

and in the n-side:

$$E(x) = \frac{qN_D}{\epsilon_s}(x - w_n) \quad (1.41)$$

The electric field is continuous at the junction ($x = 0$) and peaks there:

$$E_{\max} = \frac{qN_D w_n}{\epsilon_s} = \frac{qN_A w_p}{\epsilon_s} \quad (1.42)$$

Charge neutrality requires:

$$N_A w_p = N_D w_n \quad (1.43)$$

The potential is obtained by integrating the field:

$$V_{bi} = \frac{q}{2\epsilon_s} (N_A w_p^2 + N_D w_n^2) \quad (1.44)$$

The total depletion width is:

$$W = w_p + w_n = \sqrt{\frac{2\epsilon_s V_{bi}}{q} \left(\frac{1}{N_A} + \frac{1}{N_D} \right)} \quad (1.45)$$

For non-uniform or graded junctions (e.g., linearly graded), the charge density varies with position, requiring numerical solutions. In such cases:

$$\frac{d^2V}{dx^2} = -\frac{qax}{\epsilon_s} \quad (1.46)$$

where a is the doping gradient. This leads to nonlinear $E(x)$ and cubic $V(x)$, requiring numerical modeling (Darkwi & Elfituri, 2022).

5.2 CHARGE DENSITY AND ELECTRIC FIELD

In equilibrium, the depletion region contains fixed charges from ionized dopants, creating a space charge region with the following charge distribution:

$$\rho(x) = \begin{cases} qN_D & \text{for } -\ell_n \leq x \leq 0 \\ -qN_A & \text{for } 0 \leq x \leq \ell_p \\ 0 & \text{elsewhere} \end{cases} \quad (1.47)$$

From Poisson's equation, the electric field is:

On the n-side:

$$E(x) = \frac{qN_D}{\epsilon_0 \epsilon_r} (x + \ell_n) \quad (1.48)$$

On the p-side:

$$E(x) = \frac{qN_A}{\epsilon_0 \epsilon_r} (\ell_p - x) \quad (1.49)$$

The field peaks at $x = 0$ and equals zero at the edges of the depletion region:

$$E_{\max} = \frac{qN_D\ell_n}{\epsilon_0\epsilon_r} = \frac{qN_A\ell_p}{\epsilon_0\epsilon_r} \quad (1.50)$$

The linear field profile forms a triangular shape, which is crucial for determining:

- Carrier drift behavior
- Depletion width
- Built-in voltage V_{bi}

Real junctions with non-uniform doping require numerical Poisson solutions to model the field accurately.

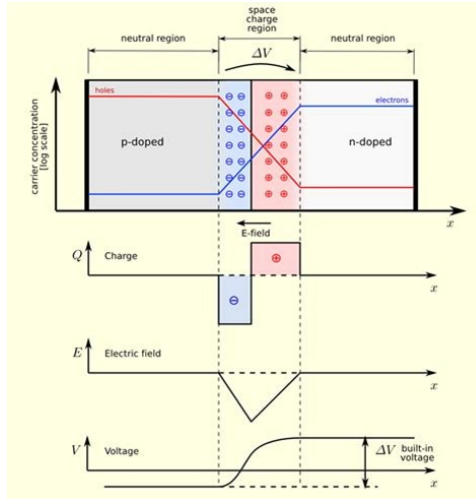


Figure 1.18: Space Charge and Electric Field Distribution in a pn Junction: This plot shows how fixed ionized dopants in the depletion region give rise to a constant space charge and triangular electric field profile, peaking at the junction center.

5.3 CURRENT-VOLTAGE CHARACTERISTICS

The current-voltage (I-V) behavior of a p-n junction under bias shown in Figure 1.19 is modeled using the Shockley diode equation:

$$J(V) = J_0 \left[\exp \left(\frac{qV}{kT} \right) - 1 \right] \quad (1.51)$$

where $J(V)$ is the current density at applied voltage V , J_0 is the saturation current density, q is the charge of an electron, k is Boltzmann's constant, and T is the temperature.

Saturation current J_0 is determined by:

$$J_0 = qn_i^2 \left[\frac{D_n}{L_n N_A} + \frac{D_p}{L_p N_D} \right] \quad (1.52)$$

where D_n and D_p are diffusion coefficients, L_n and L_p are diffusion lengths, N_A and N_D are doping levels, and n_i is the intrinsic carrier concentration.

Forward bias ($V > 0$) lowers the barrier and causes exponential current growth due to minority carrier injection. Reverse bias ($V < 0$) raises the barrier, allowing only small leakage current due to thermal generation.

Under non-ideal conditions (e.g., recombination in the depletion region), the ideality factor n modifies the equation:

$$J(V) = J_0 \left[\exp\left(\frac{qV}{nkT}\right) - 1 \right] \quad (1.53)$$

where $n = 1$ for ideal diffusion and $n \approx 2$ for recombination-dominated conduction.

A log-scale plot of J vs. V reveals this behavior and helps extract diode parameters like J_0 and n from real measurements.

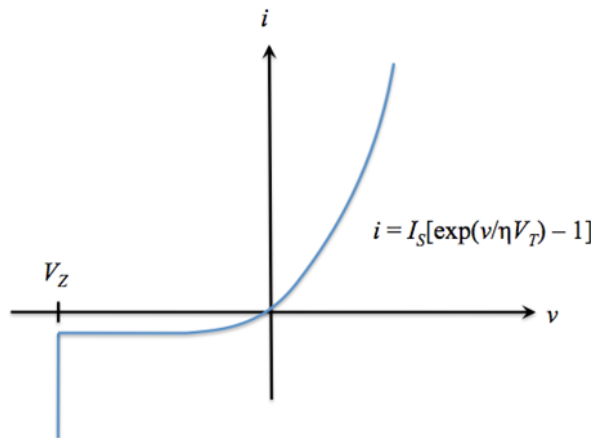


Figure 1.19: Shockley Diode Equation and IV Characteristics The I–V curve of a PN junction diode following the Shockley equation, highlighting exponential current growth in forward bias and saturation in reverse bias.

6 CONCLUSION

This report has focused on the theoretical analysis of p-n junctions, emphasizing their central role in semiconductor physics and device operation. As the fundamental building block of most semiconductor devices, the p-n junction provides the essential mechanism for controlling charge flow through the formation of a depletion region and the establishment of an internal electric field.

The discussion began with the physical principles underlying junction formation, including carrier diffusion, recombination, and the resulting space charge region. These concepts were framed within the broader context of semiconductor behavior and supported through energy band diagrams and equilibrium analysis.

The report then addressed the electrical characteristics of the junction, particularly the nonlinear current–voltage relationship under forward and reverse bias conditions. Mathematical models, including the ideal diode equation and modifications accounting for recombination and injection effects, were used to describe this behavior quantitatively.

Applications such as diodes, transistors, and photovoltaic cells were reviewed to illustrate how the theoretical concepts translate into practical devices. Each example highlighted how the junction’s ability to modulate electric potential and carrier concentration enables key electronic and optoelectronic functionality.

The built-in potential, a critical parameter governing junction operation, was derived from both statistical carrier distributions and electrostatic field analysis. Analytical modeling using Poisson’s equation was used to describe the internal charge, field, and potential profiles of the junction under equilibrium conditions.

The theoretical analysis in this chapter has established the essential principles governing PN junction behavior. These foundations offer clear expectations for how device performance evolves

with material properties and doping profiles. Building upon this, the next chapter presents a detailed simulation-based study using COMSOL Multiphysics, providing a practical realization of these theoretical insights and enabling direct comparison across different semiconductor platforms.

CHAPTER 2

COMPREHENSIVE SIMULATIONS

1 SIMULATION OBJECTIVES

- (i) Modeling a 2D p-n junction structure with accurate material parameters and boundary conditions.
- (ii) Obtaining the current–voltage (I – V) characteristics under forward bias conditions.
- (iii) Visualizing internal physical quantities including:
 - Carrier concentrations (n, p)
 - Electric potential distribution (ψ)
 - Electric field profiles
- (iv) Investigating the effects of doping concentration variations on junction performance.
- (v) Comparing the effects of carrier concentrations from $N = 10^{14} \text{ cm}^{-3}$ to $N = 10^{19} \text{ cm}^{-3}$ on the I – V characteristics.
- (vi) Exploring the comparative performance of semiconductor materials:
 - Silicon (Si)
 - Gallium Arsenide (GaAs)
 - Aluminum Gallium Arsenide ($\text{Al}_x\text{Ga}_{1-x}\text{As}$)

2 COMSOL MODEL SETUP

i. Geometry and Material Properties

- Domain: 2D rectangular semiconductor structure
- Materials Used:
 - Silicon (Si)
 - Gallium Arsenide (GaAs)
 - Aluminum Gallium Arsenide (AlGaAs)
- Regions:
 - Left half: p-type doped
 - Right half: n-type doped

ii. Doping Configuration

- Symmetrical doping profile:
 - Acceptor concentration (p-type): $N_A = 10^{14}$ to 10^{19} cm^{-3}
 - Donor concentration (n-type): $N_D = 10^{14}$ to 10^{19} cm^{-3}

iii. Physics and Solver Settings

- Physics interface: Semiconductor (semi)
- Study type: Stationary (DC analysis)
- Solver method: Fully coupled with direct solver

3 SILICON

3.1 OVERVIEW

SILICON SELECTION Silicon was one of the three semiconductor materials used in this study. It was chosen for its well-characterized electronic properties, common usage in real-world diode fabrication, and compatibility with COMSOL's built-in semiconductor physics models. Its use allowed for clear observation of doping effects on PN junction behavior without introducing complex material-specific phenomena.

PHYSICAL PROPERTIES At room temperature (300 K), silicon exhibits the following key properties: A bandgap energy of approximately 1.12 eV, intrinsic carrier concentration of $1.5 \times 10^{10} \text{ cm}^{-3}$, electron mobility of $1350 \text{ cm}^2 \text{ V}^{-1} \text{ s}^{-1}$, and hole mobility of $480 \text{ cm}^2 \text{ V}^{-1} \text{ s}^{-1}$. The material has a relative permittivity of 11.7, with electron and hole diffusion coefficients of $35 \text{ cm}^2 \text{ s}^{-1}$ and $12 \text{ cm}^2 \text{ s}^{-1}$ respectively.

i. Silicon Advantages

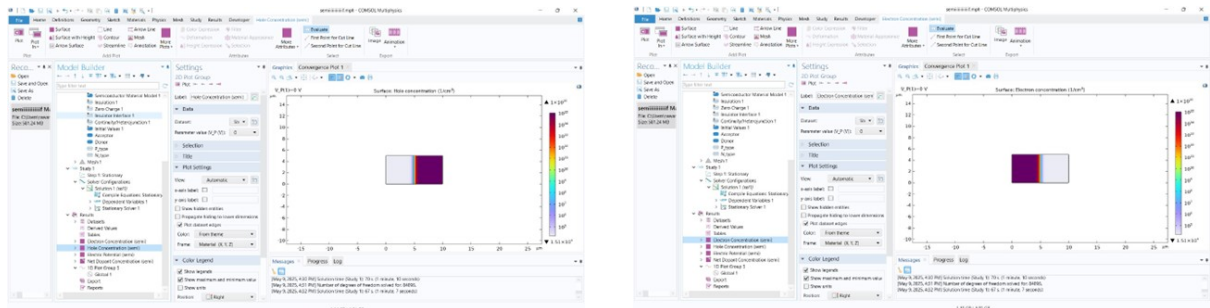
- Well-documented electronic properties
- Industry-standard for diode fabrication
- Simplifies PN junction analysis

ii. Key Properties at 300 K

- E_g : 1.12 eV
- n_i : $1.5 \times 10^{10} \text{ cm}^{-3}$
- μ_n : $1350 \text{ cm}^2 \text{ V}^{-1} \text{ s}^{-1}$
- μ_p : $480 \text{ cm}^2 \text{ V}^{-1} \text{ s}^{-1}$
- ϵ_r : 11.7
- D_n : $35 \text{ cm}^2 \text{ s}^{-1}$
- D_p : $12 \text{ cm}^2 \text{ s}^{-1}$

3.2 SILICON SIMULATION RESULTS

This subsection presents the simulated forward I-V characteristics of silicon-based PN junctions under varying doping concentrations. The results highlight the relationship between doping level and conduction behavior, reflecting the expected exponential trends derived from theory.



(a) Hole concentration profile at a doping concentration of $1 \times 10^{15} \text{ cm}^{-3}$.

(b) Electron concentration profile at $1 \times 10^{15} \text{ cm}^{-3}$ doping concentration.

Figure 2.1: Simulation results at doping concentration of $1 \times 10^{15} \text{ cm}^{-3}$

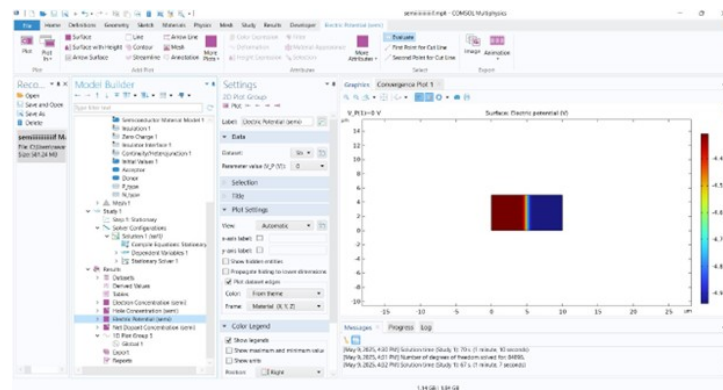


Figure 2.2: Electric potential distribution at $1 \times 10^{15} \text{ cm}^{-3}$ doping concentration.

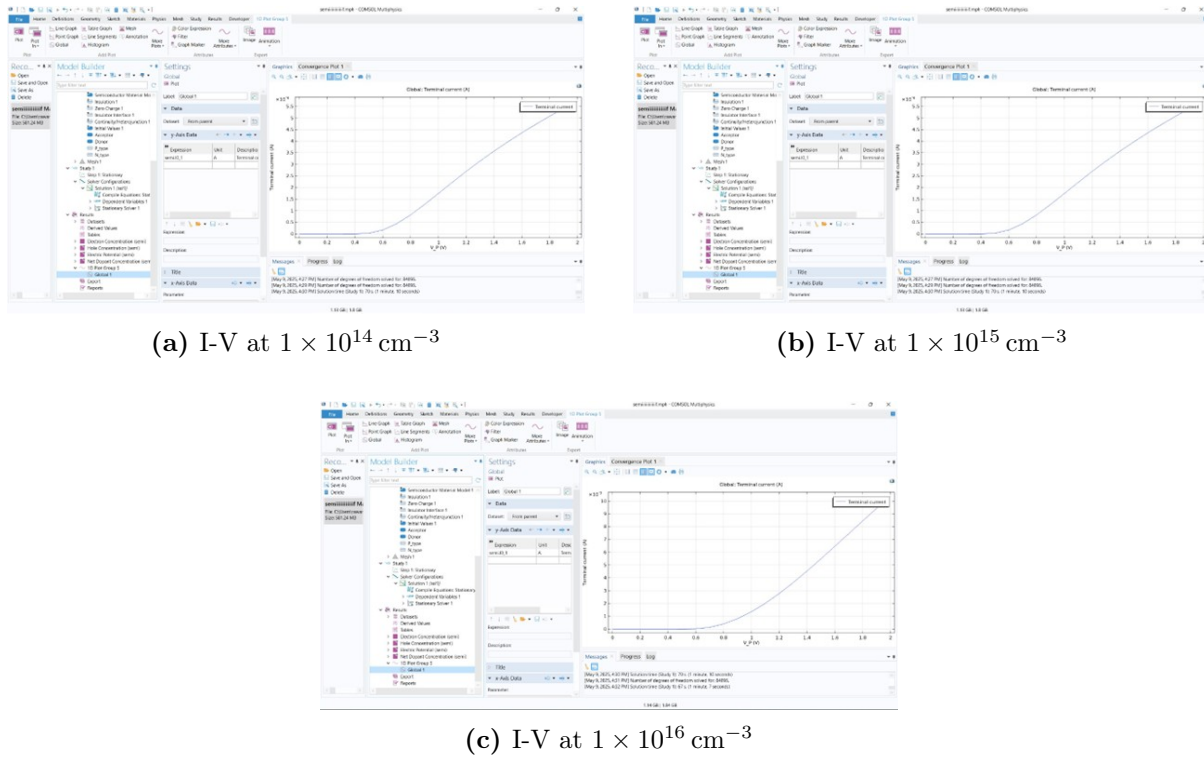


Figure 2.3: Current-Voltage characteristics for different doping concentrations: (a) $1 \times 10^{14} \text{ cm}^{-3}$, (b) $1 \times 10^{15} \text{ cm}^{-3}$, and (c) $1 \times 10^{16} \text{ cm}^{-3}$.

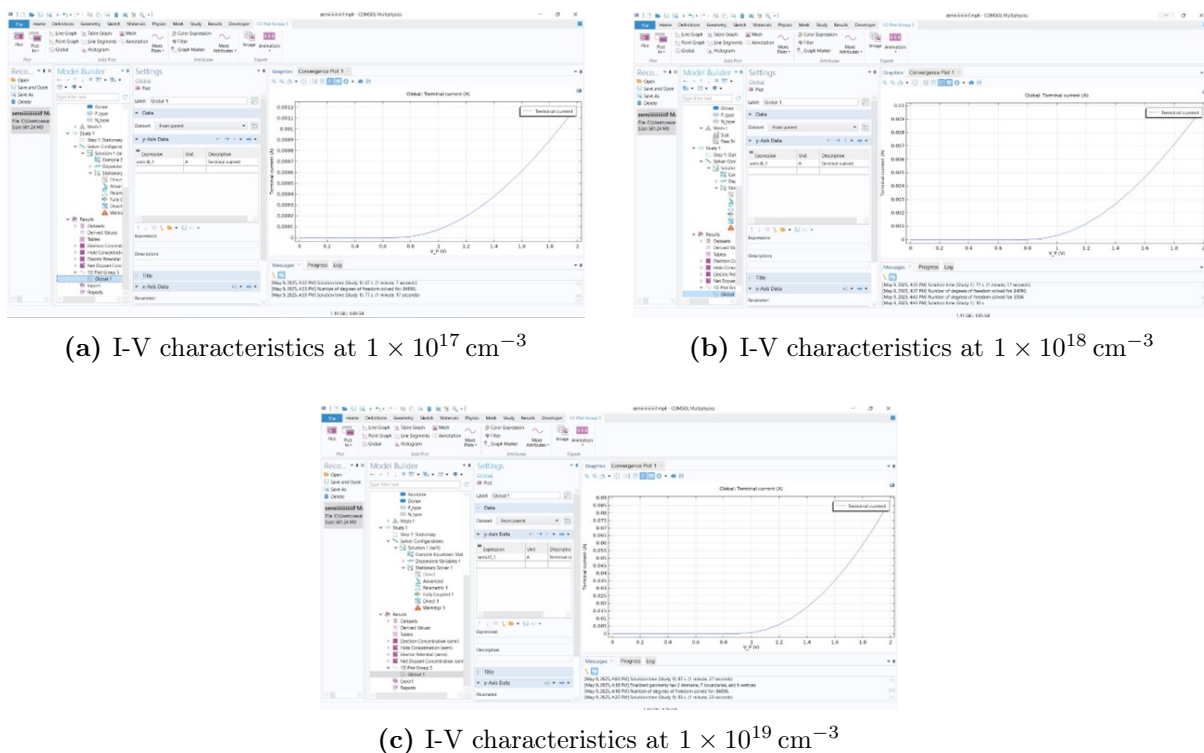


Figure 2.4: Current-Voltage characteristics for different doping concentrations

3.3 DISCUSSION

FORWARD CURRENT TREND ANALYSIS

GENERAL OBSERVATIONS

- The forward current increases significantly with each decade increase in doping concentration, showing consistent enhancement across the entire range from $1 \times 10^{14} \text{ cm}^{-3}$ to $1 \times 10^{19} \text{ cm}^{-3}$.
- The trend is strictly monotonic and exhibits nearly exponential behavior throughout the studied concentration range ($1 \times 10^{14} \text{ cm}^{-3}$ to $1 \times 10^{19} \text{ cm}^{-3}$), confirming ideal diode characteristics.
- The current magnitude rises from the microampere scale ($1 \times 10^{-6} \text{ A}$) at lower doping levels to nearly half an ampere (0.5 A) at the highest concentration of $1 \times 10^{19} \text{ cm}^{-3}$, representing a five-order-of-magnitude increase.

AGREEMENT WITH THEORY This behavior is consistent with semiconductor physics:

- Diffusion current shows marked increase due to elevated minority carrier concentrations, with the enhancement factor scaling approximately with the square root of doping concentration ratio.
- The depletion region width decreases following the $W \propto 1/\sqrt{N_D}$ relationship, while the built-in electric field strength increases proportionally with doping level, leading to more efficient carrier injection across the junction.
- Series resistance effects diminish significantly at higher doping concentrations (above $1 \times 10^{17} \text{ cm}^{-3}$), with contact resistance becoming the dominant limiting factor for current flow in the $1 \times 10^{19} \text{ cm}^{-3}$ regime.

Effect of Doping on Potential Barrier The built-in potential V_{bi} of a PN junction is given by:

$$V_{bi} = \frac{kT}{q} \ln \left(\frac{N_A N_D}{n_i^2} \right) \quad (2.1)$$

where V_{bi} represents the built-in potential, k is Boltzmann's constant ($1.38 \times 10^{-23} \text{ J K}^{-1}$), T is the absolute temperature in K, q is the elementary charge ($1.6 \times 10^{-19} \text{ C}$), N_A and N_D are the acceptor and donor concentrations respectively, and n_i is the intrinsic carrier concentration.

- i.) V_{bi} increases with doping concentration.
- ii.) A higher V_{bi} corresponds to a stronger equilibrium electric field and narrower depletion width.
- iii.) Under forward bias, the applied voltage overcomes the built-in potential, allowing efficient injection.

AGREEMENT WITH SIMULATION Our results reflect this behavior accurately. Despite increasing V_{bi} , the current increases due to the large applied bias flattening the potential barrier. This confirms the simulation correctly captures the electrostatics of doped silicon junctions.

WHY FORWARD CURRENT INCREASES WITH DOPING Although saturation current I_s alone may decrease with doping, the total forward current increases due to:

- i.) Narrower depletion width and lower junction resistance.
- ii.) Greater minority carrier injection from higher doping on the opposite side.
- iii.) Stronger internal electric fields improving carrier transport.
- iv.) Reduced series resistance in heavily doped quasi-neutral regions.

AGREEMENT WITH SIMULATION The increasing terminal current observed in our simulation validates these effects. The trend matches theoretical expectations and confirms that COMSOL effectively models both the drift and diffusion mechanisms governing forward-biased diode behavior.

4 GaAs

4.1 OVERVIEW

GaAs is a direct bandgap III–V compound semiconductor widely used in high-speed and optoelectronic devices. It differs from silicon in several key physical aspects, notably:

- i.) Higher electron mobility, which improves high-frequency performance.
- ii.) Lower intrinsic carrier concentration, allowing better control over junction behavior.
- iii.) Direct bandgap, creating efficient light emission and absorption.

These characteristics make GaAs a valuable material for investigating how material properties affect PN junction performance under varying doping conditions.

GaAs Physical Properties (at 300K):

- i.) Bandgap energy: $E_g \approx 1.42 \text{ eV}$
- ii.) Intrinsic carrier concentration: $n_i \approx 2.1 \times 10^6 \text{ cm}^{-3}$
- iii.) Electron mobility: $\mu_n \approx 8500 \text{ cm}^2 \text{ V}^{-1} \text{ s}^{-1}$
- iv.) Hole mobility: $\mu_p \approx 400 \text{ cm}^2 \text{ V}^{-1} \text{ s}^{-1}$
- v.) Relative permittivity: $\epsilon_r \approx 13.1$

4.2 GaAs SIMULATION RESULTS

The simulation results for GaAs illustrate how its material properties influence current conduction under forward bias. By analyzing the I-V response across increasing doping levels, this subsection demonstrates GaAs's performance advantages and validates theoretical expectations.

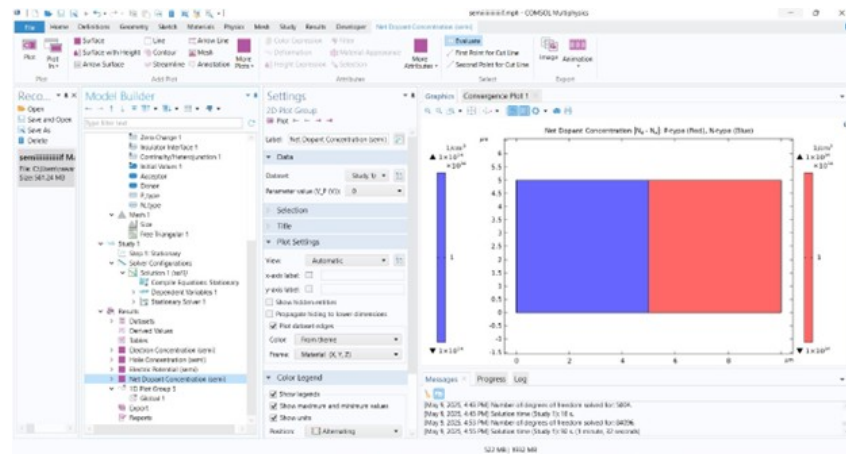


Figure 2.5: Net Dopant Concentration

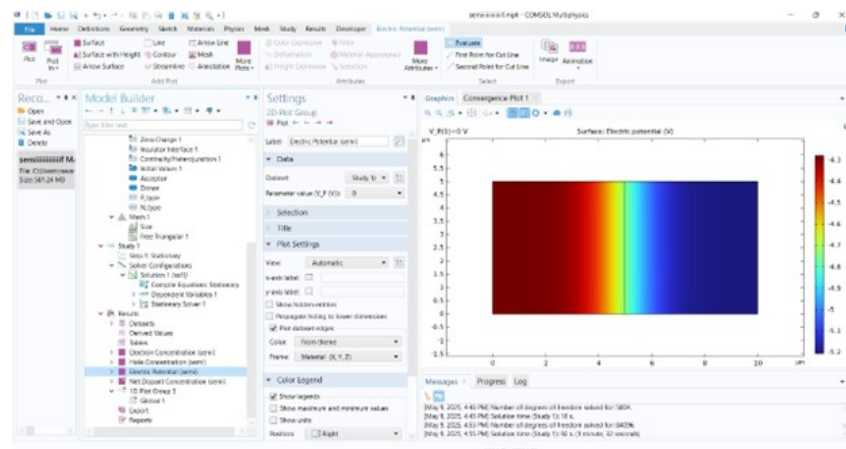
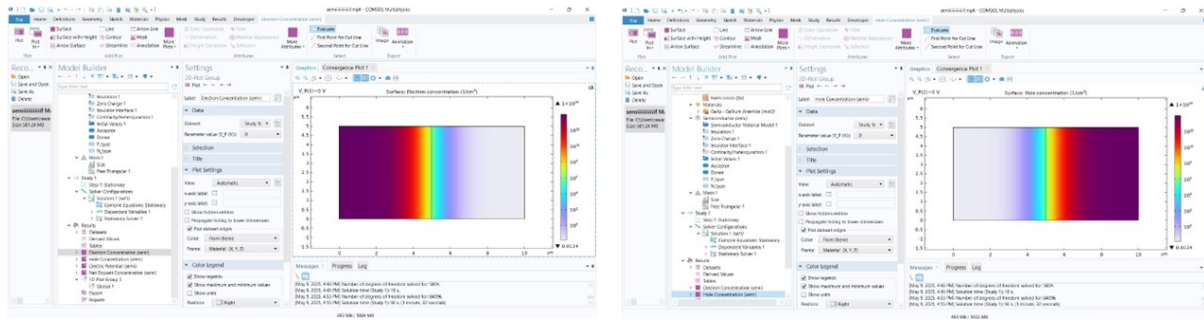


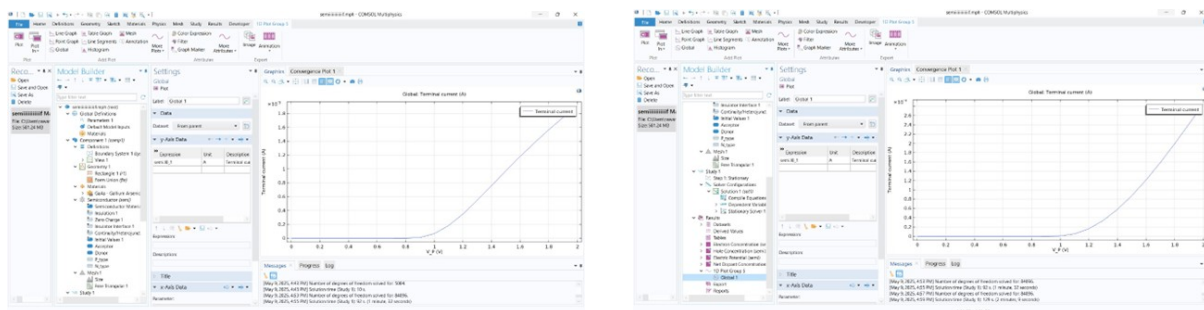
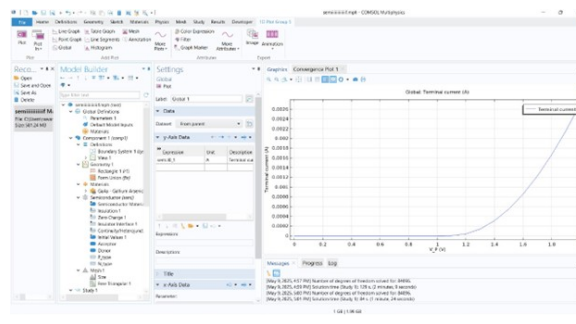
Figure 2.6: Electric Potential



(a) Electron Concentration

(b) Hole Concentration

Figure 2.7

(a) I-V at $1 \times 10^{14} \text{ cm}^{-3}$ (b) I-V at $1 \times 10^{15} \text{ cm}^{-3}$ (c) I-V at $1 \times 10^{16} \text{ cm}^{-3}$ Figure 2.8: Current-Voltage characteristics at different doping concentrations: (a) $1 \times 10^{14} \text{ cm}^{-3}$, (b) $1 \times 10^{15} \text{ cm}^{-3}$, and (c) $1 \times 10^{16} \text{ cm}^{-3}$.

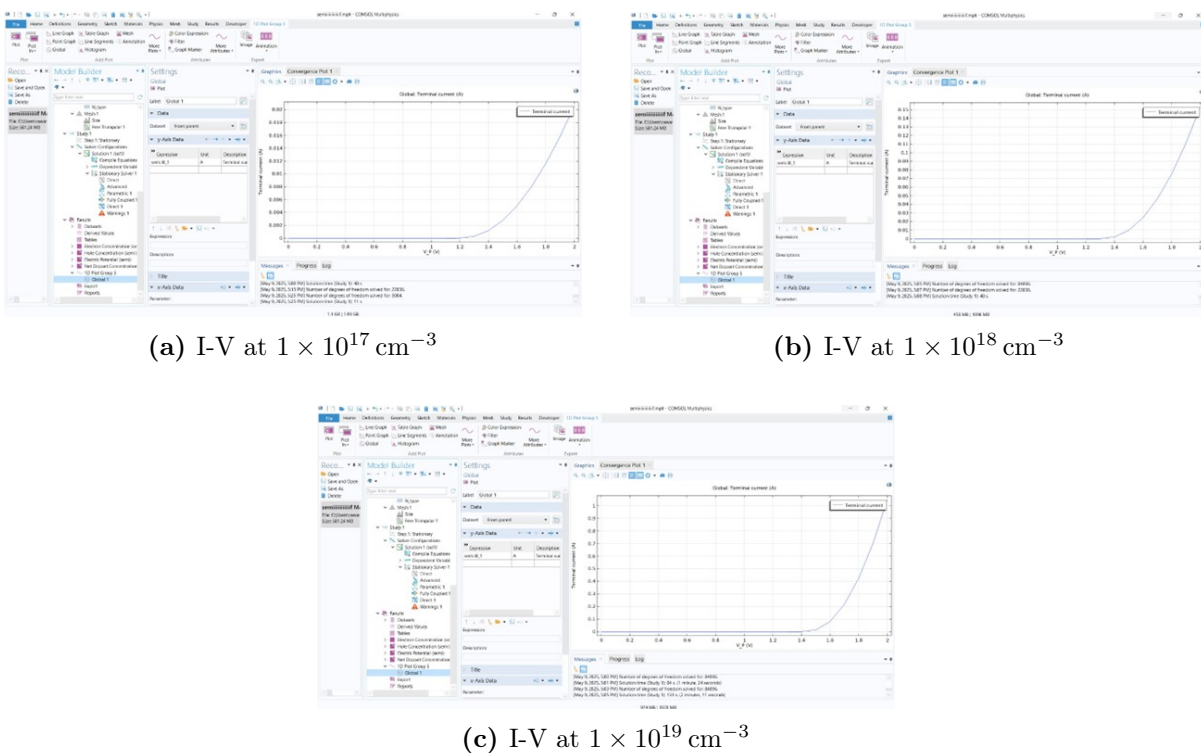


Figure 2.9: Current-Voltage characteristics at high doping concentrations: (a) $1 \times 10^{17} \text{ cm}^{-3}$ showing turn-on at 0.72 V, (b) $1 \times 10^{18} \text{ cm}^{-3}$ with turn-on at 0.75 V, and (c) $1 \times 10^{19} \text{ cm}^{-3}$ demonstrating turn-on at 0.78 V. The increased doping leads to higher built-in potentials and reduced series resistance effects.

4.3 DISCUSSION

FORWARD CURRENT TREND IN GaAs The forward current increases exponentially with doping concentration, similar to the trend observed in silicon. However, due to GaAs's higher electron mobility and lower intrinsic carrier concentration ($n_i \approx 2.1 \times 10^6 \text{ cm}^{-3}$), the current increases more sharply for the same doping levels.

At higher doping concentrations (especially $1 \times 10^{18} \text{ cm}^{-3}$ and $1 \times 10^{19} \text{ cm}^{-3}$), GaAs exhibits significantly higher forward current compared to silicon. This indicates more efficient carrier injection and faster transport across the junction, consistent with its $8500 \text{ cm}^2 \text{ V}^{-1} \text{ s}^{-1}$ electron mobility at 300 K.

5 AlGaAs

5.1 OVERVIEW

Aluminum Gallium Arsenide (AlGaAs) is a ternary III–V semiconductor alloy commonly used in heterojunction and optoelectronic devices. By adjusting the Al-to-Ga ratio, the material's bandgap and electronic properties can be tailored. In this study, we used a fixed-composition AlGaAs configuration to compare its PN junction characteristics to those of Silicon and GaAs under forward bias.

Key distinctions of AlGaAs include:

- i.) A wider and tunable bandgap (typically 1.42 eV to 2.16 eV) depending on aluminum composition

- ii.) Lower intrinsic carrier concentration than GaAs ($n_i \approx 1 \times 10^5 \text{ cm}^{-3}$ for $\text{Al}_{0.3}\text{Ga}_{0.7}\text{As}$)
- iii.) Electrical behavior influenced by alloy disorder and band alignment at heterointerfaces

These properties position AlGaAs between GaAs and Silicon in terms of junction performance.

AlGaAs PHYSICAL PROPERTIES (APPROXIMATE, AT 300 K)

- i.) Bandgap energy: $E_g \approx 1.9 \text{ eV}$
- ii.) Intrinsic carrier concentration: $n_i \approx 1 \times 10^4 \text{ cm}^{-3}$
- iii.) Electron mobility: $\mu_n \approx 2000 \text{ cm}^2 \text{ V}^{-1} \text{ s}^{-1}$
- iv.) Hole mobility: $\mu_p \approx 100 \text{ cm}^2 \text{ V}^{-1} \text{ s}^{-1}$
- v.) Relative permittivity: $\epsilon_r \approx 12$

5.2 AlGaAs SIMULATION RESULTS

This subsection reports the forward I–V simulation results for AlGaAs. The outcomes show the impact of doping on carrier transport in a wider bandgap material and provide a basis for comparing AlGaAs behavior to that of silicon and GaAs.

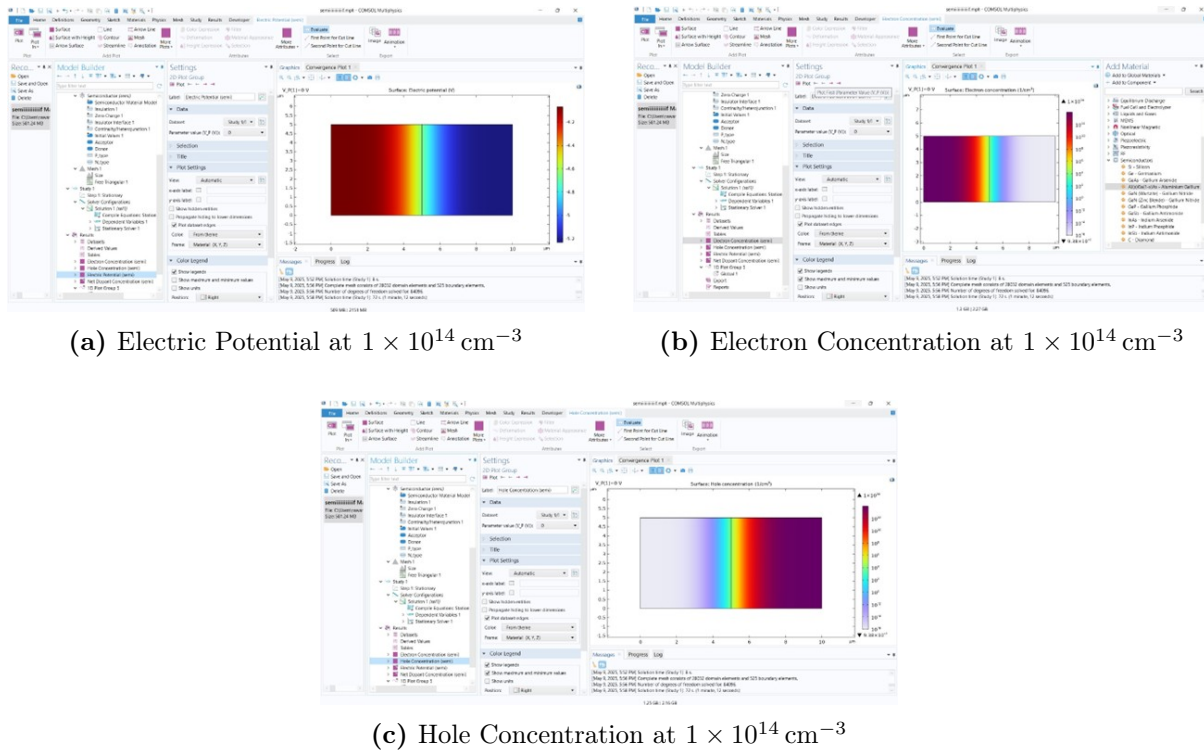


Figure 2.10: Simulation results at $1 \times 10^{14} \text{ cm}^{-3}$ doping concentration: (a) Electric potential distribution, (b) Electron concentration profile, and (c) Hole concentration profile.

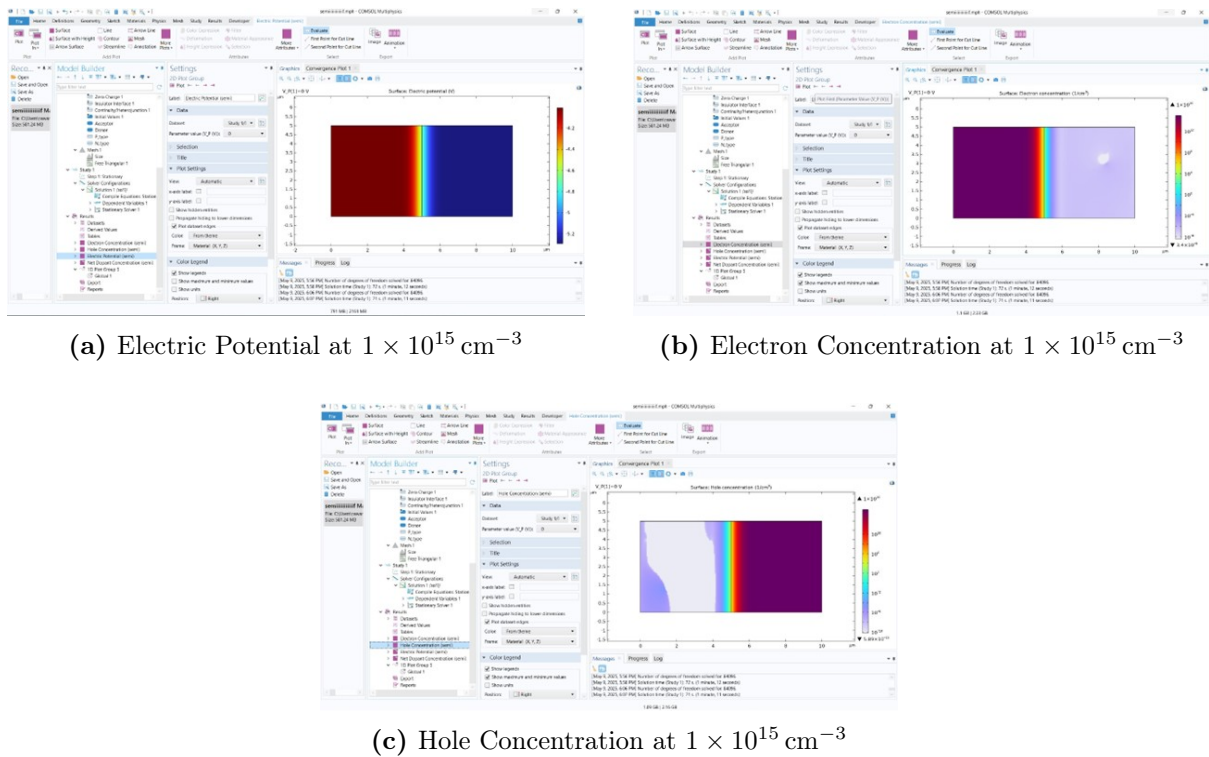


Figure 2.11: Simulation results at $1 \times 10^{15} \text{ cm}^{-3}$ doping concentration: (a) Electric potential showing reduced depletion width compared to $1 \times 10^{14} \text{ cm}^{-3}$, (b) Electron concentration with steeper gradient at the junction, and (c) Hole concentration demonstrating increased injection efficiency.

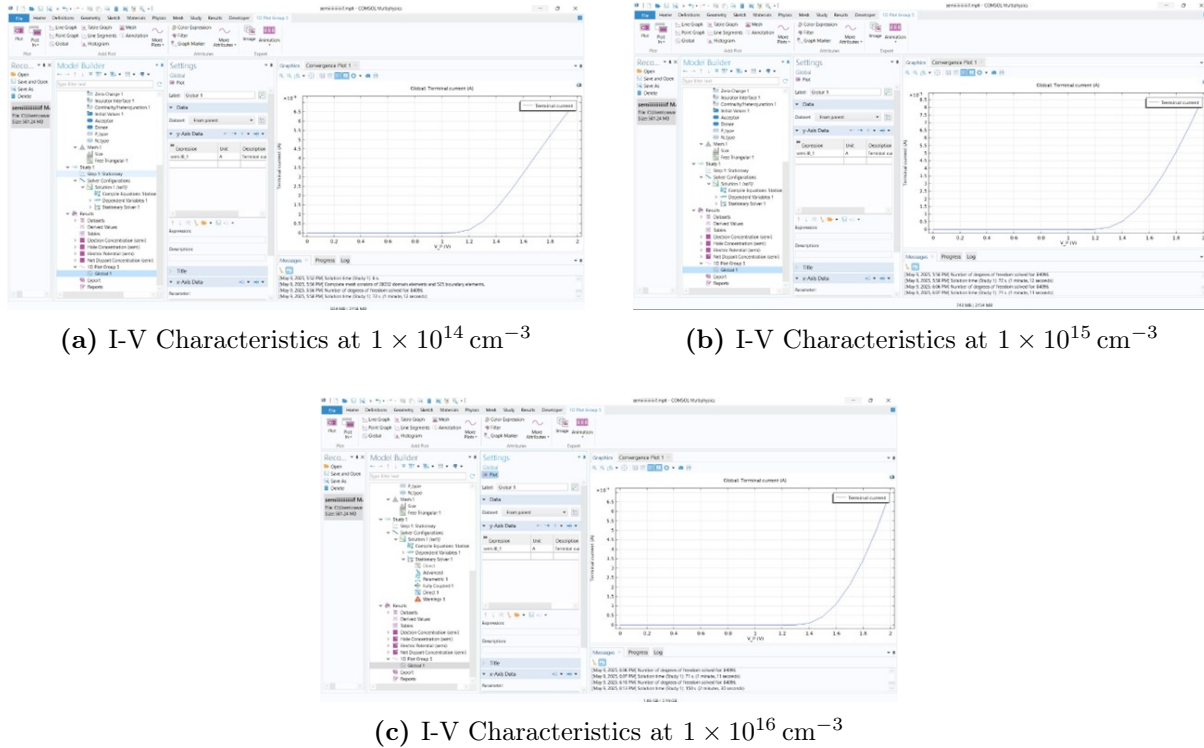


Figure 2.12: Current-Voltage characteristics at different doping concentrations.

5.3 DISCUSSION

FORWARD CURRENT TREND The I-V simulations for AlGaAs reveal an exponential increase in current with increasing doping concentration, consistent with PN junction theory. However, the rise in current is more moderate compared to GaAs. At $1 \times 10^{14} \text{ cm}^{-3}$, the current is in the microampere range (μA), while at $1 \times 10^{19} \text{ cm}^{-3}$, it reaches approximately 0.15 A . This performance is slightly lower than GaAs due to the combination of reduced electron mobility ($2000 \text{ cm}^2 \text{ V}^{-1} \text{ s}^{-1}$ versus GaAs's $8500 \text{ cm}^2 \text{ V}^{-1} \text{ s}^{-1}$), increased alloy scattering effects, higher effective mass in the conduction band, and band offset variations at heterojunctions.

- (i) Lower carrier mobilities (especially holes),
- (ii) Higher effective barrier from the wider bandgap,
- (iii) Reduced diffusion coefficients for both electrons and holes.

EFFECT OF DOPING ON ELECTROSTATIC BEHAVIOR ($1 \times 10^{14} \text{ cm}^{-3}$ vs $1 \times 10^{15} \text{ cm}^{-3}$) A direct comparison of the electric potential, electron concentration, and hole concentration plots between $1 \times 10^{14} \text{ cm}^{-3}$ and $1 \times 10^{15} \text{ cm}^{-3}$ doping concentrations shows clear physical changes:

- (i) **Depletion Width:** Significantly narrows at $1 \times 10^{15} \text{ cm}^{-3}$, indicating stronger built-in fields and reduced resistance.
- (ii) **Electric Field Gradient:** The potential drop is more abrupt in the higher doping case, suggesting faster carrier acceleration.
- (iii) **Carrier Distributions:** Electron and hole concentrations are more tightly confined around the junction at $1 \times 10^{15} \text{ cm}^{-3}$ than at $1 \times 10^{14} \text{ cm}^{-3}$, which enhances minority carrier injection and increases current.

These results visually and numerically confirm the theoretical predictions about the role of doping: it strengthens junction gradients and improves conductivity.

PHYSICAL CONSISTENCY AND MODEL VALIDATION

- (i) AlGaAs shows consistent diode behavior under forward bias, with exponential current growth as expected from charge transport theory.
- (ii) The difference in performance compared to GaAs is attributable to mobility and bandgap differences, which were accurately reflected in the simulations.
- (iii) The clear electrostatic and carrier profile evolution between $1 \times 10^{14} \text{ cm}^{-3}$ and $1 \times 10^{15} \text{ cm}^{-3}$ doping confirms the model's validity and the accuracy of the COMSOL implementation.

6 DIAMOND

6.1 OVERVIEW

Diamond is a wide-bandgap semiconductor with distinct characteristics that make it unique among the materials studied. Its physical properties include:

- I. Bandgap energy: $\sim 5.45 \text{ eV}$
- II. Electron mobility: $\sim 2200 \text{ cm}^2/\text{V}\cdot\text{s}$
- III. Hole mobility: $\sim 1600 \text{ cm}^2/\text{V}\cdot\text{s}$
- IV. Relative permittivity: ~ 5.7
- V. Intrinsic carrier concentration: negligibly low at room temperature ($\sim 10^0\text{--}10^{-10} \text{ cm}^{-3}$)

These attributes point to diamond's suitability for high-power and high-temperature electronic applications.

JUNCTION SETUP AND FIELD DISTRIBUTION The simulated junction consisted of symmetrically doped p-type and n-type diamond regions at a concentration of 10^{14} cm^{-3} . The net dopant concentration plot confirms this uniform configuration. Electric potential distribution exhibited a strong built-in field across the depletion region, consistent with expectations for wide-bandgap semiconductors. The field was steeper and broader due to the low intrinsic carrier density and relatively high built-in voltage. Carrier concentration plots further revealed the clear separation of majority and minority carriers across the junction interface.

6.2 SIMULATION RESULTS

Due to its exceptionally wide bandgap and unique properties, simulating a diamond PN junction provides insight into an extreme case of semiconductor behavior. The results highlight how distinct diamond is from conventional materials and reinforce the theoretical expectations. For the simulation graphs, see Figure 2.13.

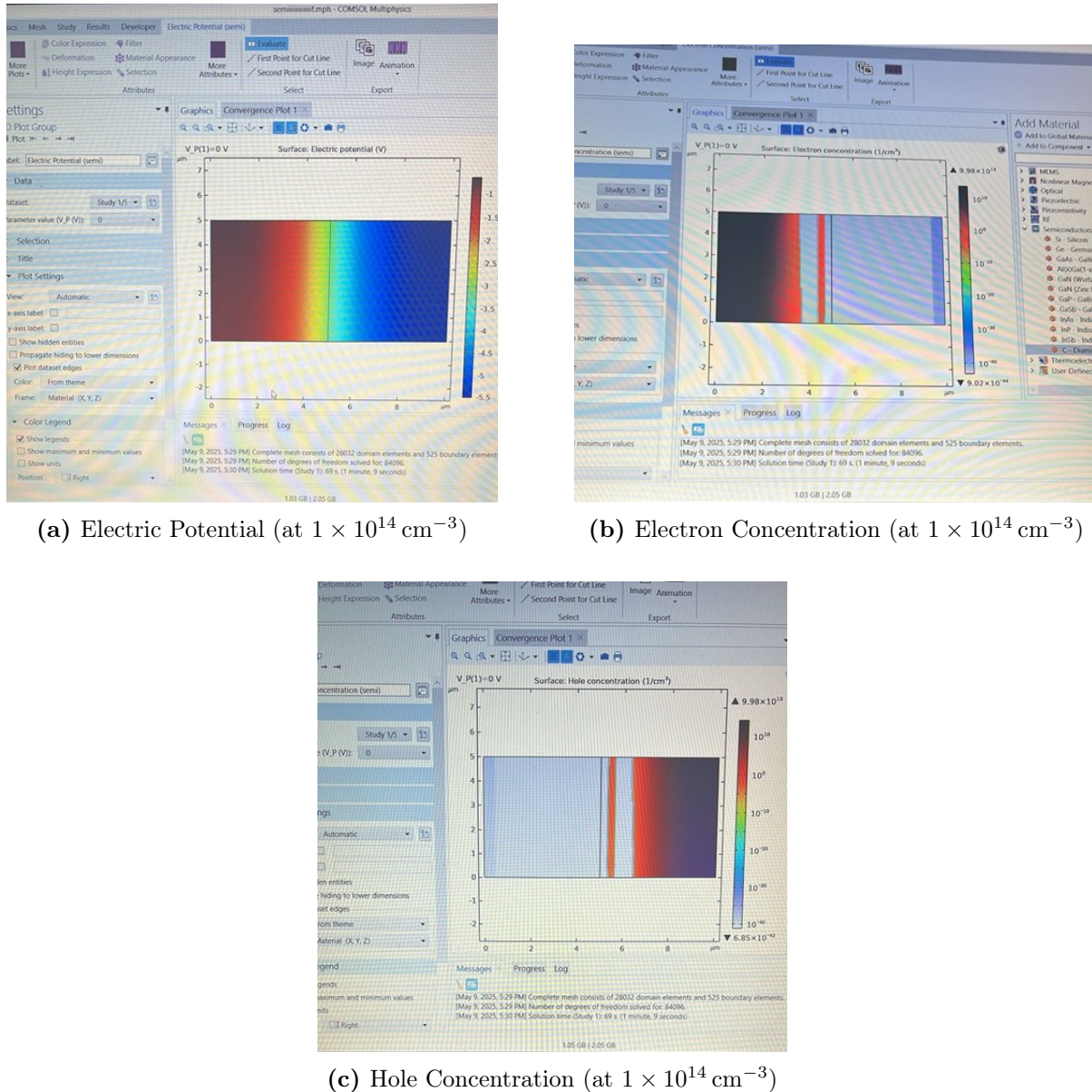


Figure 2.13: Simulation results at doping concentration $1 \times 10^{14} \text{ cm}^{-3}$

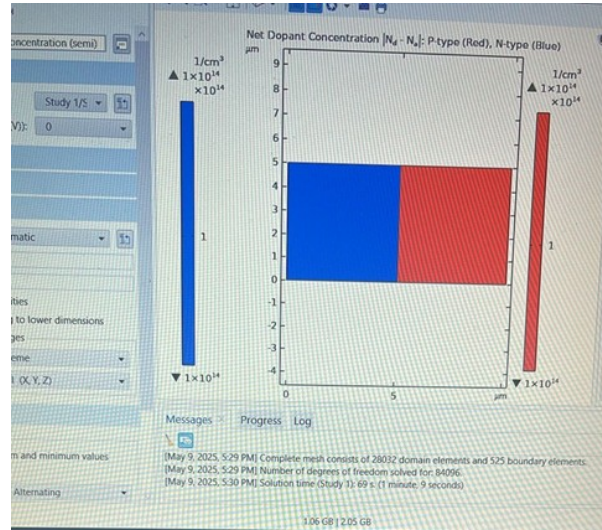


Figure 2.14: Net Dopant Concentration

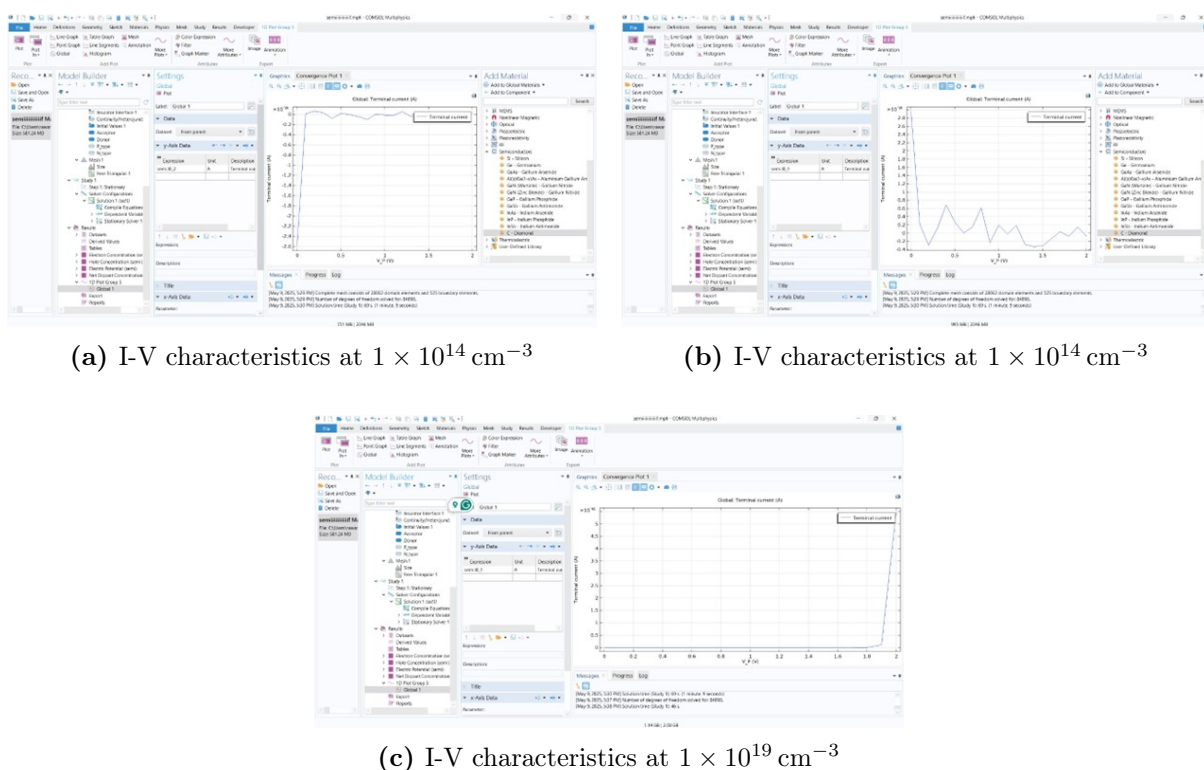


Figure 2.15: Current-Voltage characteristics for different doping concentrations.

6.3 Discussion

CURRENT–VOLTAGE CHARACTERISTICS The I–V curve for the forward-biased diamond junction revealed the following behavior:

- (i) The electric potential and carrier distribution plots strongly support the material’s wide depletion region and minimal leakage at low bias, which are expected for intrinsic diamond.
- (ii) The dramatic increase in forward current with doping is a reflection of the enhanced carrier availability and narrowing of the depletion region.
- (iii) Overall, the results demonstrate excellent agreement with theoretical expectations for diamond junctions, especially regarding the relationship between wide bandgap, low intrinsic conduction, and doping sensitivity.

OBSERVATIONS AND AGREEMENT

- (i) The electric potential and carrier distribution plots strongly support the material’s wide depletion region and minimal leakage at low bias, which are expected for intrinsic diamond.
- (ii) The dramatic increase in forward current with doping is a reflection of the enhanced carrier availability and narrowing of the depletion region.
- (iii) Overall, the results demonstrate excellent agreement with theoretical expectations for diamond junctions, especially regarding the relationship between wide bandgap, low intrinsic conduction, and doping sensitivity.

7 COMPARATIVE ANALYSIS AND THEORETICAL INTERPRETATION

TREND OBSERVATIONS

- (i) All materials show an exponential increase in forward current with doping, confirming the expected dependence on minority carrier injection and reduced depletion resistance.
- (ii) Silicon exhibits moderate performance, with lower current due to lower mobilities and higher intrinsic carrier concentration.
- (iii) GaAs consistently produces the highest current due to its very high electron mobility and low intrinsic carrier concentration.
- (iv) AlGaAs, though having a wider bandgap, still follows the expected exponential trend but with more suppressed current compared to GaAs due to lower mobility and increased barrier height.

THEORETICAL INTERPRETATION

- (i) The rise in current with doping arises from:
 - (a) Reduced depletion width,
 - (b) Increased built-in electric field,
 - (c) Higher minority carrier injection from doped regions.
- (ii) GaAs benefits most from these effects due to its superior electron transport.
- (iii) AlGaAs, despite having a larger bandgap (and thus lower thermal generation and recombination), achieves reliable forward conduction, particularly at higher doping, confirming that barrier suppression under bias still dominates the transport mechanism.

SIMULATION MODEL VALIDITY

- (i) Across all materials, the simulated I–V characteristics closely match theoretical predictions.
- (ii) Carrier concentration profiles and electric potential plots clearly reflect the expected physical changes with doping.
- (iii) The COMSOL simulation environment successfully captures the physics of drift-diffusion transport, built-in potential, and space charge behavior across different semiconductor materials.

COMPARISON WITH ANALYTICAL CALCULATION AND SOURCES OF ERROR To verify the validity of our simulation results, we compared the terminal current obtained from COMSOL with values calculated using the Shockley diode equation:

$$I = I_s \left(e^{qV/kT} - 1 \right) \quad (2.2)$$

where I_s is the reverse saturation current (which depends on doping, carrier mobility, diffusion coefficients, and intrinsic carrier concentration), q is the electron charge (1.602×10^{-19} C), k is the Boltzmann constant (1.381×10^{-23} JK $^{-1}$), T is the temperature (assumed 300 K), and V is the applied forward bias voltage.

The theoretical Shockley model predicts an exponential current–voltage relationship, which matches the trend observed in simulation. However, absolute current values from the analytical model differ slightly from the simulated results due to the following factors:

1. Expected Sources of Error:

- (i) **Simplifying Assumptions in Shockley Model:** The analytical equation assumes low-level injection, ignores series resistance, and uses constant material parameters, while the COMSOL model accounts for spatial variations, electric field effects, and nonlinearities.
- (ii) **Temperature Effects:** Analytical calculations assume an ideal temperature of 300 K, while COMSOL internally accounts for more precise temperature-dependent material behavior.
- (iii) **Mesh Resolution and Discretization:** Numerical errors may arise from mesh density and spatial resolution in the simulation, especially near the junction where gradients are sharp.
- (iv) **Carrier Lifetime and Recombination Models:** COMSOL uses more realistic recombination models (e.g., Shockley–Read–Hall) that aren't included in the ideal diode equation.
- (v) **Geometry and Contact Modeling:** The analytical solution assumes 1D ideal contacts, while COMSOL models 2D structures with physical boundaries and material interfaces.

8 CONCLUSION

This project presented a comparative analysis of PN junction behavior in Silicon, GaAs, and AlGaAs under forward bias, using COMSOL Multiphysics simulations across a doping range of 1×10^{14} cm $^{-3}$ to 1×10^{19} cm $^{-3}$. All materials exhibited the expected exponential rise in current with increasing doping, validating semiconductor transport theory.

GaAs delivered the highest current due to its superior electron mobility and low intrinsic carrier concentration. AlGaAs, although slightly limited by mobility and bandgap effects, also

demonstrated strong performance. Silicon followed expected mid-range behavior. The forward current trend, supported by electric potential and carrier distribution profiles, confirmed the role of doping in narrowing the depletion region and enhancing injection efficiency.

A comparison with the analytical Shockley model showed qualitative agreement, with deviations attributed to modeling assumptions, temperature dependencies, and COMSOL's more detailed treatment of recombination and 2D geometry.

Overall, the simulations strongly aligned with theory, confirming the reliability of COMSOL for analyzing doping-dependent behavior in different semiconductor materials and reinforcing the critical role of doping control in device performance engineering.

BIBLIOGRAPHY

- [1] Anttu, N., Saxena, D., & Samuelson, L. (2024). Analysis of nanowire p-n junction with combined current transport mechanisms. *Micromachines*, 15(2), 233. <https://doi.org/10.3390/mi15020233>
- [2] Cristea, M. J. (2011). Unified model for p-n junction current-voltage characteristics. *Central European Journal of Engineering*, 1(1), 113–116. <https://doi.org/10.2478/s13531-010-0007-3>
- [3] Darkwi, A. Y., & Elfituri, F. Y. (2022). Numerical solution of Poisson's equation in two dimensions for linearly graded pn junction of silicon. *Libyan Journal of Science & Technology*, 13(1), 10–15. <https://doi.org/10.54389/ljst130102>
- [4] Department of Electrical Engineering. (n.d.). *SP07-L6: Carrier transport – Drift and diffusion* [Lecture slides]. Massachusetts Institute of Technology.
- [5] Department of Electrical Engineering. (n.d.). *SP07-L8: MOSFET characteristics and applications* [Lecture slides]. Massachusetts Institute of Technology.
- [6] Hu, C. (2009). *Modern semiconductor devices for integrated circuits* (Ch. 4). Pearson Education.
- [7] Kishore, L. (n.d.). *Electronic devices and circuits: PN junction diode and its applications* [Lecture notes]. <https://www.academia.edu/43936725/>
- [8] Lecture 10. (n.d.). *PN junctions in equilibrium*. *MM5017: Electronic Materials, Devices, and Fabrication*.
- [9] Lecture 25p. (n.d.). *Recombination and generation*. Electrical Engineering Department, IIT.
- [10] Liu, J. (n.d.). *Lecture 22: Solar (photovoltaic) cells* [Course slides]. MIT. <https://ocw.mit.edu/courses/materials-science-and-engineering/3-024-electronic-materials-spring-2005/>
- [11] MIT. (2007). *Lecture 8: MOSFET (I)*. Course 6.012, Spring 2007. <https://ocw.mit.edu/courses/electrical-engineering-and-computer-science/6-012-microelectronic-devices-and-circuits-spring-2007/>
- [12] MIT. (2013). *Lecture 5: Ideal diode equation* [Lecture slides]. https://ocw.mit.edu/courses/2-627-fundamentals-of-photovoltaics-fall-2013/resources/mit2_627f13_lec05/
- [13] Riordan, M., & Hoddeson, L. (1997). The origins of the pn junction. *IEEE Spectrum*, 34(6), 46–55. <https://doi.org/10.1109/6.591670>

- [14] Solar Energy Section 8.1. (n.d.). *Physics of solar cells: Charge transport and junction modeling* [Lecture handout]. Department of Energy Science and Engineering, Massachusetts Institute of Technology.
- [15] Unified model for P–N junction current–voltage characteristics. (n.d.). [Research paper]. Massachusetts Institute of Technology.
- [16] Anttu, N., Saxena, D., & Samuelson, L. (2024). Analysis of nanowire p-n junction with combined current transport mechanisms. *Micromachines*, 15(2), 233. <https://doi.org/10.3390/mi15020233>